Simulations of a silicon vertex tracker for a future EIC

eRD18

H. Wennlöf*, L. Gonella, P.G. Jones, P.P. Allport, P.R. Newman

*h.l.o.wennlof@pgr.bham.ac.uk

University of Birmingham
School of Physics and Astronomy
February 2020

Contents

1 Introduction

The EIC is a new experimental facility recently approved to be built at the Brookhaven National Laboratory. The facility will enable collisions of polarised beams of electrons and ions, with a centre-of-mass energy range of 20 to 140 GeV. Reserach and development towards an EIC detector has been ongoing for the past ten years, with different detector concepts being investigated. Currently there are four different suggested designs for a detector; the BeAST (Brookhaven eA Solenoidal Tracker) [1], the JLEIC [2], ePHENIX [3], and TOPSiDE (Time-of-flight Optimized PID Silicon Detector for the EIC) [4]. The different concepts are shown schematically in Figure 1.
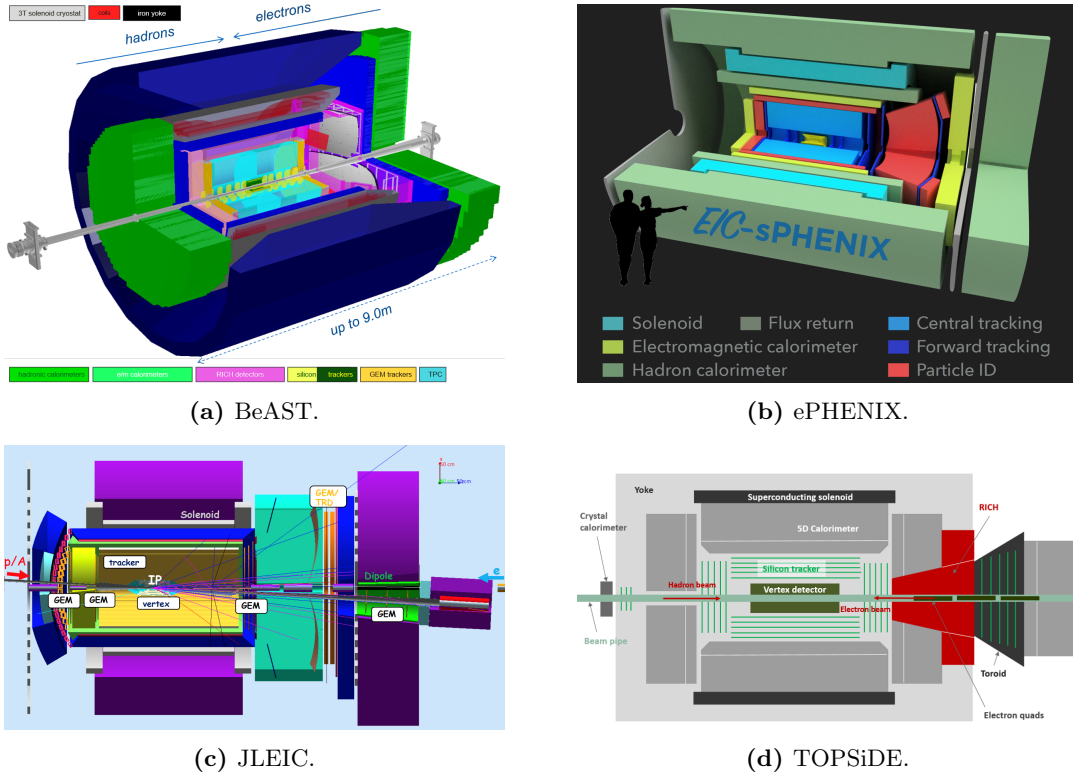

(a) BeAST.

(b) ePHENIX.

(c) JLEIC.

(d) TOPSiDE.

Figure 1: The four current detector concepts developed for the EIC [1].

Broadly, the detector concepts are similar. BeAST and ePHENIX are developed at BNL, while JLEIC is developed at JLAB. TOPSiDE is an all-silicon detector concept, developed at the Argonne National Laboratory. All four detector concepts have a silicon vertex tracker closest to the interaction point. This is the focus of the project presented here, making it largely independent of the concept finally selected.

To examine the effects of the layout of a full silicon vertex tracker, with some given constraints on material thickness, simulations are made. In the work carried out in this project, a combination of the ALICE Inner Tracker upgrade [5] and the inner tracker of the BeAST detector is used as a baseline. At the silicon vertex tracker level however, all the detector concepts are similar. The simulations described in this section will thus be valid for any of the concepts. Small adjustments will have to be made depending on the details of the detector and the beampipe, but the results of the simulations will be largely applicable to any of the concepts.

The purpose of the simulations is to determine the most efficient silicon vertex tracker layout, with respect to resolution of momentum and point of origin (vertex position) of the tracked particles. In the EIC, the vertex position is of interest, as heavy flavour particles will be created in the collision and decay within a short distance ($\sim$100 μm) from the collision vertex. It is thus

3

important to be able to reconstruct the point of origin for the tracked particles, and be able to separate the primary collision vertex from the secondary decay vertex to accurately describe the physics of the collision. The momentum resolution is used for particle identification and separation, and is thus an important tool for event reconstruction. The figures of merit observed in the presented simulations are the relative momentum resolution and the pointing resolution, which is a measurement of how well the particle creation vertex can be found. The theory behind those figures of merit can be found in Sections A.2.2 and A.2.3.

In the simulations, a time-stamping layer is also added, to investigate the effects it would have on the resolutions. Such a layer would have the possibility of time-stamping bunch crossings, and thus help keep track of the beam polarisations in the detected interactions. The simulations study whether adding such a layer would be detrimental to the detector performance, without considering the possible benefits the time-stamping would bring to event separation and reconstruction.

2   Experimental setup

Simulations are made using EICROOT, which is a Monte Carlo framework for detector simulation specifically developed for the EIC collaboration [6]. At the time the simulations were started, this was the framework most readily available at the University of Birmingham. EICROOT is based on the PandaRoot framework, which in turn is based on the FairRoot framework [7]. The ROOT version used in the simulations is ROOT 5.34/36, and GEANT3 is used for the Monte Carlo part of the simulations.

At the start of the simulation, the detector geometry to be investigated is defined; the vertex tracker pixel size, the thickness of the detector layers, and the detector layout are selected. The parameter space for the Monte Carlo simulation is then defined; the particle type, the pseudorapidities in which the particles are generated, their generated momentum (or transverse momentum) range, and the number of events to be generated. The pseudorapidity η is defined as $\eta = -\ln(\tan(\theta/2))$, where θ is the angle of the particle relative to the beam axis. Each event consists of one particle, created at the centre of the defined geometry, with momentum that places it within the defined parameter space. The particles are created using a version of the `EicBoxGenerator`, modified to create a uniform distribution in transverse momentum p_T or momentum p. A magnetic field is also defined to be uniformly 1.5 T or 3 T along the beam direction in the detector. The 1.5 T field is the same as the field in the existing BaBar solenoid, and the suggested solenoid for the ePHENIX concept [3]. A solenoid with a field of 3 T is discussed in the EIC White Paper [8], and in the JLEIC concept [9].

The Monte Carlo simulation is performed for the geometry and parameters given, creating and propagating particles through the detector. The information about the propagation of the particle is saved, and makes up a "true track" that the particle has taken. Details of the interaction of the particle with the geometry is also saved, and where it hit the sensitive areas of the detector.

The detector hits are then digitised, with a smearing around the hit position determined by a selected pixel size. The pixels in the vertex tracker are defined to be square, and the smearing is Gaussian with a standard deviation given by the pixel side length divided by $\sqrt{12}$ (see Section A.2.1). The smeared hit positions are stored.

A reconstruction is then made, using the digitised hits on the active detector area. A Kalman filter is used as part of an ideal tracker using the digitised detector hits [10]. This forms a reconstructed track.

Finally, analysis code is executed to compare the simulated "true track" to the reconstructed track. This makes it possible to compare parameters of the tracks, and thus see how good the defined detector is at reconstructing the truth. In particular, the relative momentum resolution and the pointing resolution are studied in the transverse plane. This plane is perpendicular to the magnetic field, so it is the plane in which the tracked particles curve, making it relevant for momentum measurements. The relative momentum resolution is found by comparing generated and reconstructed transverse momenta, and extracting the resolution at different momentum values by fitting a Gaussian to the distributions at those values. For the transverse pointing resolution, the reconstructed vertex position in the transverse plane (x and y, given that z is the beam direction) is treated in the same way for different values of the momentum. The same is also done for the longitudinal pointing resolution (in the z direction).

The interval used for the Gaussian fit is set to 1.5 standard deviations around the peak centre position. This range was deemed to be the best way of extracting data reliably from the central peak, avoiding the tails of the distributions. More information concerning this can be found in Appendix B.

The particles used in the simulations presented here are positive pions, π^+, in the barrel region. Pions are used because they have hadronic interactions, and are a decay product of the D^0 which is an interesting charmed meson in this context. At higher pseudorapidities (more forward regions), electrons are used instead of pions as the scattered electron is the main particle of

investigation in those regions. The pseudorapidity range investigated is $-0.5 \leq \eta \leq 0.5$ for the central barrel studies (using pions), $\eta = 3$ for the silicon disk studies, and $0 \leq \eta \leq 2.5$ for the simulations using both barrel and disks.

Where not otherwise stated, all simulations contain the same beampipe configuration in the centre, made up of beryllium, with a radius of 18 mm and a thickness of 0.8 mm. Outside the varied silicon vertex tracker is a time projection chamber (TPC). This starts at a radial distance of 225 mm from the centre, and ends at a radial distance of 775 mm. The TPC has a length of 1960 mm along the beam axis, and is centred around the "interaction point" where the simulated particles are created.

Between the beampipe and the TPC the silicon vertex tracker is situated. This is the main detector part under investigation. The structure of layers in the tracker is based on the ALICE Inner Tracker upgrade design [5]. The innermost layers thus have a thickness of (in radiation lengths, see Section A.1.1) 0.3 % X_0, and the outer layers 0.8 % X_0.

The starting point for the inner tracker geometry is the BeAST vertex tracker. This tracker consists of four layers; two of the inner layer types for the ALICE upgrade, and two of the outer layer types. The positioning of these layers is modified from the standard BeAST layout to match the spacing of the upgraded ALICE inner tracking system [5]. This ensures that the layout is physically viable when support structures and services are included in the construction. The inner layers have a length in the beam direction of 270 mm, and the outer layers have a length of 840 mm. The innermost layer is placed at a radius of 23.4 mm (i.e. 23.4 mm from the centre of the beampipe, where the particles are created in the simulations), and consists of 12 staves of chips, tilted by 12 degrees to have an overlap to cover the full area. The second layer is at a radius of 46.8 mm, and consists of 24 staves. The third layer is of the ALICE outer cell type, with a thickness of 0.8 % X_0. It is located at a radius of 87.6 mm, and consists of 10 staves. The outer cell staves are wider than the inner ones, and hence fewer staves are needed to cover the full area. The fourth and outermost layer consists of 16 staves, and resides at a radius of 133.8 mm. This leaves space for a time-stamping layer, located at a radius of 180.0 mm.

Where not otherwise stated, the time-stamping layer has a thickness twice that of an outer barrel layer, i.e. 1.6 % X_0, and a pixel size matching the rest of the barrel. The increased thickness stems from that a higher time resolution will require a higher power to the chips in the layer. This means that more cooling is needed to keep the layer operational, and the material thickness will thus increase. Larger pixels might also be needed to accommodate the circuitry needed for the time-stamping, and to keep power density low. Results of investigations of different thicknesses and pixel sizes for the time-stamping layer are presented in Section 3.5.

In the forward and backward regions of the detector, silicon disks are placed. This is discussed in more detail in Sections 3.6 through 3.9.

Figure 2 shows a sketch of the simulated detector, with the different silicon vertex tracker barrel layer distances marked. A time-stamping layer is also present, as the outermost line in the barrel part of the sketch. A basic disk layout consisting of 7 disks in the forward region and 7 disks in the backward region is also shown in the sketch. In Section 3.4 the radiation lengths of the different detector parts are shown as a function of pseudorapidity.

For the variations in silicon vertex tracker barrel layout, the innermost and outermost layers are kept the same, while the middle two layers are varied.

Simulations were first performed focusing on the silicon vertex tracker barrel. The region in the interface between the barrel and the silicon disks was later studied as well, and finally the possibility of an all-silicon tracker replacing the gas TPC was investigated. The results are presented below in that order.
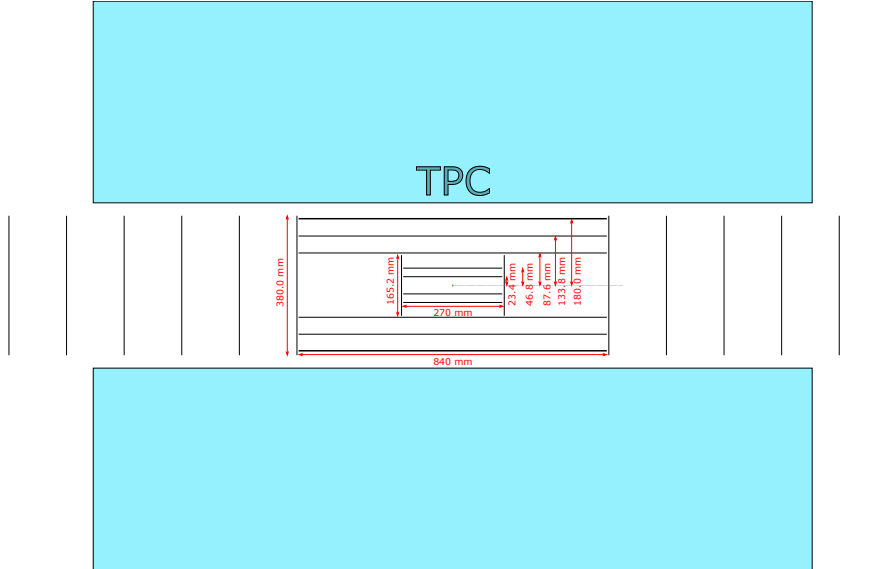
Figure 2: Sketch of the simulated silicon vertex tracker barrel, with surrounding TPC and silicon disks. A beampipe runs through the centre of the detector, but is left out of the figure.

3   Results

The resolutions shown are the relative momentum resolution and the transverse pointing resolution for the discussed detector variations. The longitudinal (beam direction) pointing resolution is also investigated, but its results often mimic those of the transverse pointing resolution, and the longitudinal pointing resolution plots are in those cases not presented.

3.1   Comparison no SVT/SVT+TPC

First of all, a study of the impact of having a silicon vertex tracker is investigated. The parameters for the simulations are shown below.

- Particle: π^+

- Transverse momentum range: 0 to 50 GeV/c

- Pseudorapidity range: $-0.5 \leq \eta \leq 0.5$

- Number of events: 100 000

- 5 layer barrel (two inner, two outer, one time-stamping layer)

- Magnetic field: 1.5 T

For the run with no silicon vertex tracker, the TPC inner radius is extended to cover the otherwise empty volume. The TPC in this case thus has an inner radius of 23.4 mm and an outer radius of 775.0 mm. Figure 3 shows the resulting resolutions. It is clear from both the relative momentum resolution and the transverse pointing resolution that adding a silicon vertex tracker barrel has great benefits. Having only the TPC is better for the relative momentum resolution only at very low transverse momenta, due to multiple scattering being dominant there (and thus less material gives a better resolution). For the pointing resolution, not having a finely segmented innermost layer is clearly detrimental at all momenta.
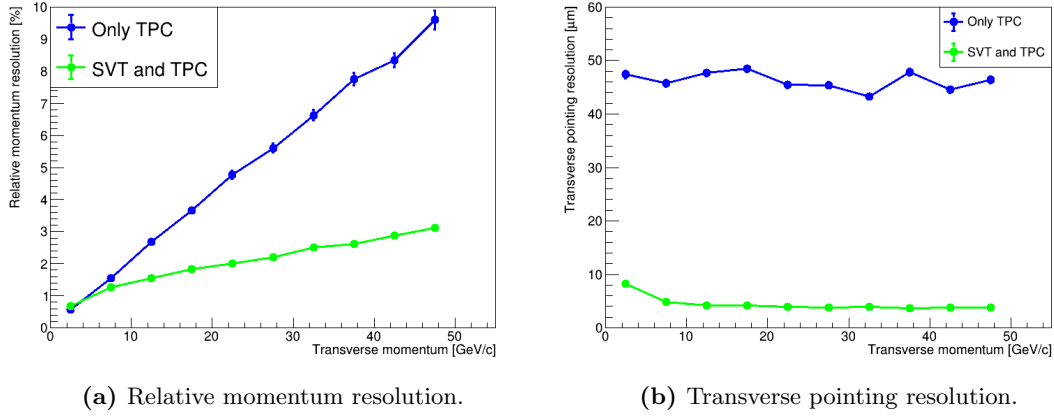
(a) Relative momentum resolution.

(b) Transverse pointing resolution.

Figure 3: Relative momentum resolution and transverse pointing resolution, comparing having a standard barrel with a 20×20 μm^2 pixel size with a TPC outside, and just having a TPC extending all the way to the same innermost radius as the barrel.

3.2   Barrel pixel size

For investigating the effect of pixel size in the barrel region on the resolutions, the parameters below are used.

- Particle: π^+
- Transverse momentum range: 0 to 5 GeV/c
- Pseudorapidity range: $-0.5 \leq \eta \leq 0.5$
- Number of events: 100 000
- 5 layer barrel (two inner, two outer, one time-stamping layer)
- Magnetic field: 1.5 T
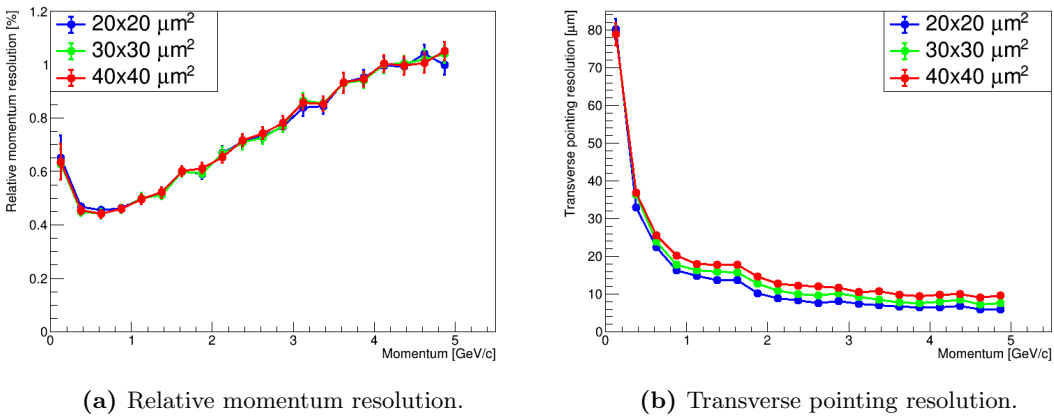
Results of varying the pixel size are shown in Figure 4.

(a) Relative momentum resolution.

(b) Transverse pointing resolution.

Figure 4: Relative momentum resolution and transverse pointing resolution for different pixel sizes in the silicon vertex tracker barrel.

The results for the pointing resolutions are in agreement with theory (see Equation A.18); smaller pixel size improves the resolution. Equation A.20 indicates a linear dependence on pixel size for the relative momentum resolution. The equation is however derived for a detector layout with all layers having the same pixel size, whereas the simulated case has different resolution in the silicon

8

layers and the TPC. The behaviour of the relative momentum resolution might thus not match the approximate theory, as the "pixel size" is not altered in the whole detector. The discrepancy with theory might also be due to the multiple scattering part of the relative momentum resolution dominating at the relatively low momenta used in this simulation, rather than the geometric part. Studies at higher momenta indicate that the expected pixel size dependence appears there.

3.3 Barrel layout studies

Figure 5 shows the relative momentum resolution and the transverse pointing resolution for different barrel layer layouts, in a transverse momentum range of 0 to 50 GeV/c. The pixel size for all layers is kept at 20×20 μm^2, and the innermost and outermost barrel layers are always present and unchanged. The parameters used in the simulations are:

- Particle: π^+

- Transverse momentum range: 0 to 5 GeV/c, and 0 to 50 GeV/c

- Pseudorapidity range: $-0.5 \leq \eta \leq 0.5$

- Number of events: 100 000

- Pixel size: 20×20 μm^2

- Magnetic field: 1.5 T

When present, the thickness of the time-stamping layer is 1.6 % X_0, and its pixel size is 20×20 μm^2. A study of varying the thickness and pixel size of the time-stamping layer is presented in Section 3.5.

(a) Relative momentum resolution.

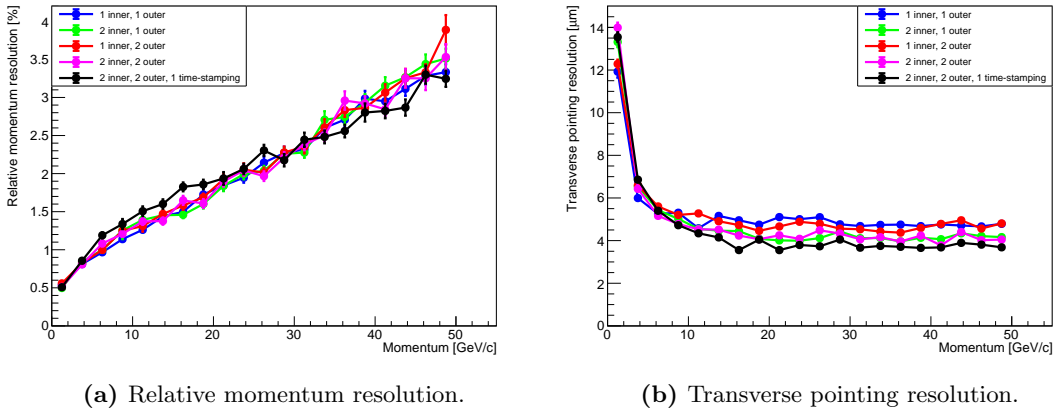(b) Transverse pointing resolution.

Figure 5: Relative momentum resolution and transverse pointing resolution for different silicon vertex tracker barrel layouts. The number of layers is varied, with the innermost and outermost layers always the same and present. Transverse momenta between 0 and 50 GeV/c.

Figure 6 is the same simulation carried out at transverse momenta between 0 and 5 GeV/c (i.e. a low transverse momentum region).

For the relative momentum resolution, there is no significant difference for the different layouts at most momenta, apart from when a time-stamping layer is present. The relative momentum resolution depends heavily on the lever arm of the detector, and since the outer and inner layers of the detector do not change, it is expected that the resolution will not change much. The standard TPC is also always present, keeping the maximum lever arm at a constant length. In Figure 6, it can be seen that after reaching a minimum the relative momentum resolution grows worse with increasing transverse momentum, which also corresponds to theory. At very low momenta, having two inner layers and only one outer layer seems to be the best (this is not seen in Figure 5, since the binning there is not as fine in the low momentum region). Multiple scattering dominates
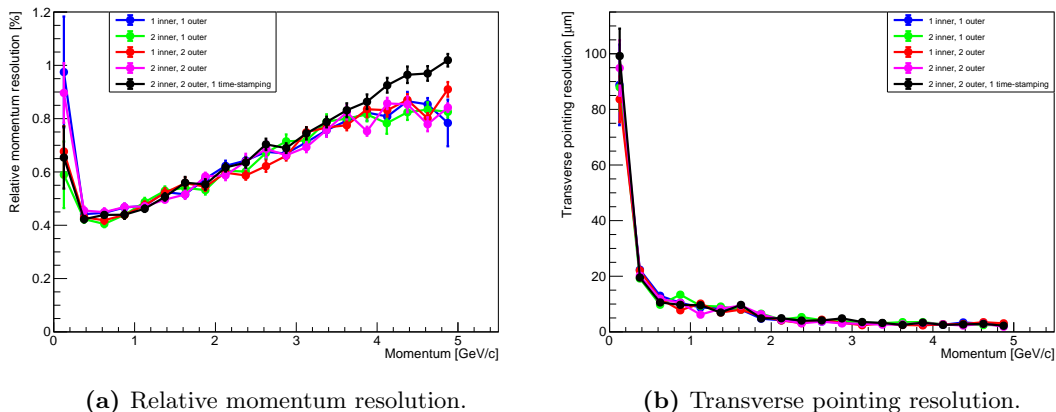
(a) Relative momentum resolution.

(b) Transverse pointing resolution.

Figure 6: Relative momentum resolution and transverse pointing resolution for different silicon vertex tracker barrel layouts. Transverse momenta between 0 and 5 GeV/c.

the resolution at low momenta, so removing material without changing the lever arm is expected to improve the resolution. The outer layers have a thickness of 0.8 % X_0 while the inner layers have a thickness of 0.3 % X_0, so removing an outer layer removes a relatively large amount of material. The measurements in this very low momentum region are of poor quality however, as particles with very low transverse momentum (below approximately 0.4 GeV/c) spiral in the magnetic field within the detector. The errors are large within this region, and the difference between several of the layouts are within errors. No strong conclusion about the optimal layout can thus be drawn from these simulations at the lowest presented momentum point.

When the time-stamping layer is present, there is a deterioration of relative momentum resolution at low momenta. This likely stems from the added material of the layer. It is equivalent to the material two outer layers would add. At higher momenta, the addition of a time-stamping layer appears to slightly improve momentum resolution. This comes from the number of layers increasing (see Equation A.20), an effect which becomes more important at higher momenta. It is however important to note that the difference in relative momentum resolution between all the tested layouts is small.

At low momenta (i.e. p_T less than 10 GeV/c), the transverse pointing resolution does not change significantly between the different geometries. This is in agreement with theory (see Equation A.18), since the total lever arm does not change, nor the distance from the beampipe to the innermost layer. At low momenta, the layouts with the lowest material close to the beampipe (i.e. just one inner layer) have marginally the best pointing resolution. At higher momenta there is a separation between the layouts, with the one containing a time-stamping layer giving the best resolution. The reason for this separation is not obvious in the parametrisation presented in Section A.2.2. The results in Figure 5 show that having two inner layers seem to be better than having one, regardless of whether there are one or two outer layers. There is possibly a dependence on the number of layers that does not show up in the theory derived from a two-layer case. There is also clearly in the equations a dependence on the lever arm for a two-layer case, with a longer arm giving better resolution. This may explain why the layout containing the time-stamping layer has the best pointing resolution at high momenta. The gas TPC is always present, keeping the maximum lever arm constant. However, the TPC has a different resolution than the silicon layers, and the silicon lever arm may have an effect separate from the lever arm given by the gas TPC.

Studies are also made looking at having the innermost layer inactive. This would be representative of a worst case scenario during operation. The results of the investigation show that there is little impact on relative momentum resolution apart from at very low momenta, but big losses in pointing resolution. An inactive innermost layer would be worse than not having the innermost layer at all, which is in agreement with theory as an inactive layer will increase multiple scattering without providing any information.

3.4   Radiation length scan

Scans are performed to determine the radiation length of the different parts of the detector used in the simulations. The standard 4-layer barrel layout is used. The plots show the radiation length plotted versus the pseudorapidity η. The resulting plots for the standard barrel with beampipe and TPC, and the same with an added time-stamping layer 1.6 % X_0 thick are shown in Figure 7. The contribuion from the TPC is split into two parts; the TPC gas (labelled "TPC_TpcGas"), and the TPC inner field cage (labelled "TPC_TpcIfc").

The different detector layers are clearly visible here, and the pseudorapidities at which they are no longer hit by a particle. There are some small irregularities present that likely stem from the tilt of the individual staves, and their overlap.
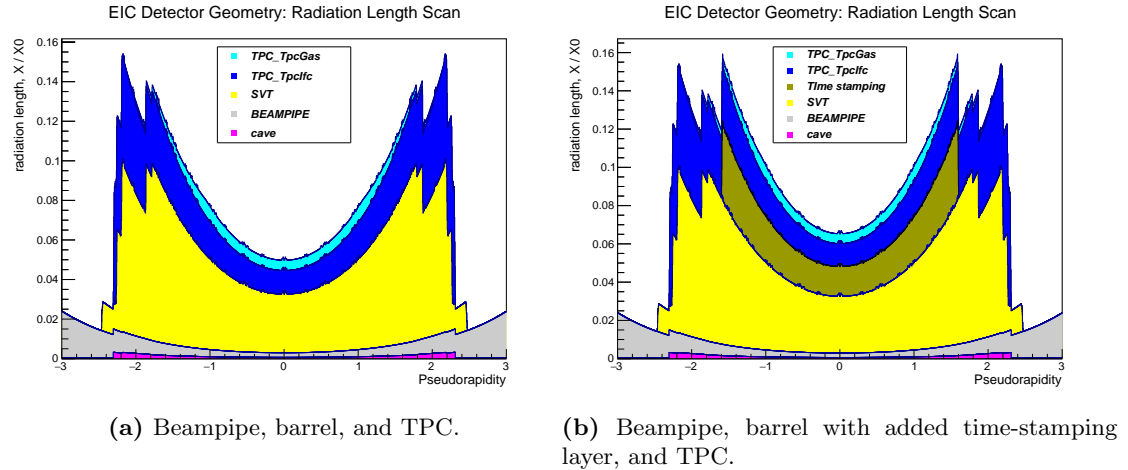

(a) Beampipe, barrel, and TPC.

(b) Beampipe, barrel with added time-stamping layer, and TPC.

Figure 7: Radiation length scans for detector setups. The standard beampipe and TPC are in place in both scans.

3.5   Time-stamping layer thickness and pixel size

Investigations are made concerning how adding a separate time-stamping layer would affect the detector performance. The standard 4-layer barrel is used, and the time-stamping layer is placed outside of it. The parameters below are used for the simulations.

- Particle: π^+
- Transverse momentum range: 0 to 5 GeV/c
- Pseudorapidity range: $-0.5 \leq \eta \leq 0.5$
- Number of events: 100 000
- Barrel pixel size: 20×20 μm^2
- Magnetic field: 1.5 T

Results for altering the time-stamping layer thickness (in terms of radiation length) are shown in Figure 8. For these studies, the time-stamping layer pixel size is kept at 20×20 μm^2.

For the time-stamping layer pixel size investigations, the thickness of the time-stamping layer is kept at 1.6 % X_0. The resulting resolutions from this investigation are shown in Figure 9.

In all the plots, the black line stems from simulations done without a time-stamping layer, and just the standard barrel with a 20×20 μm^2 pixel size. It can be seen that time-stamping layer pixel size has little to no significant impact on either of the resolutions. Adding a time-stamping layer makes both the relative momentum resolution and the transverse pointing resolution worse at very low momenta ($p_T \leq 0.4$ GeV/c). This is due to it adding a significant amount of material,
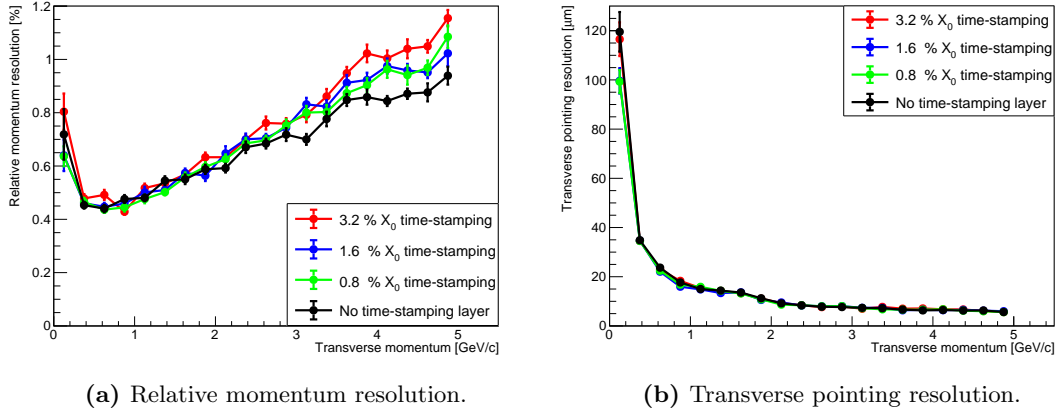
(a) Relative momentum resolution.

(b) Transverse pointing resolution.

Figure 8: Relative momentum resolution and transverse pointing resolution for different time-stamping layer thicknesses.

(a) Relative momentum resolution.
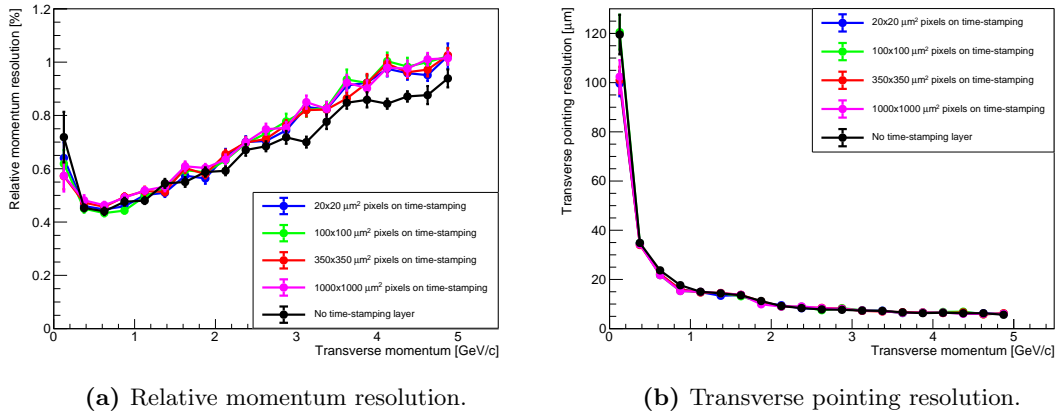
(b) Transverse pointing resolution.

Figure 9: Relative momentum resolution and transverse pointing resolution for different time-stamping layer pixel sizes.

at a thickness of 1.6 % X_0. At high momenta, the relative momentum resolution is worse when a time-stamping layer is present. This likely stems from the increase in material, which is also indicated in the time-stamping layer thickness results; it is possible to see that a thinner time-stamping layer is better for the relative momentum resolution. There is however no significant difference between having a layer that is 0.8 % X_0 thick and one that is 1.6 % X_0 thick. For the transverse pointing resolution, the time-stamping layer thickness has no significant effect above very low momenta.

3.6 Disks, varying pixel sizes

The EIC R&D group eRD16 focus mainly on the forward region of the inner tracking detector. In a collaboration with this group, silicon disks are included in the forward region of the detector in the simulations.

First of all, the resolutions are investigated in the forward region for different pixel sizes in the disks. The disks are made up of the same material as the inner barrel layers, with a thickness of 0.3 % X_0. They are placed equidistantly between 250 mm (in the beam direction) and 1210 mm from the interaction point. These distances are based on the results of a preliminary study carried out by eRD16, showing that this is a reasonable geometry for matching the silicon vertex tracker requirements.

The innermost disk is shrunk to have an outer radius of 82.6 mm, so that it fits within the outer barrel layers (with a 5 mm margin). The opening in the disk centred around the beampipe is square, with a side of 36 mm for the innermost disk, and 40 mm for the other disks.

In the forward region, the main purpose for a deep inelastic scattering experiment is to detect the scattered electron. Hence electrons are used for the studies involving disks, rather than the pions used previously. It is also preferable to reconstruct the total momentum rather than the transverse momentum of the electron, and hence the total momentum resolution is used in these studies. A uniform momentum distribution is also generated, rather than a uniform transverse momentum distribution.

For the studies of different pixel sizes in the forward region, the following parameters are used:

- Particle: e^-

- Momentum range: 0 to 50 GeV/c (uniform in p)

- Pseudorapidity: $\eta = 3$

- No barrel and no TPC present

- Number of events: 500 000

- Magnetic field: 1.5 T and 3 T

Since the pseudorapidity used is so high, there is no reason to have a silicon barrel or a TPC present in the simulations, as they will never be hit. This also means that the simulations are more light-weight, meaning a higher number of events can be simulated easily.

Simulations are done for magnetic fields of 1.5 T and 3 T. Figure 10 show the results for a field of 1.5 T, and Figure 11 show the results for a field of 3 T.

(a) Relative momentum resolution.

(b) Transverse pointing resolution.

(c) Longitudinal pointing resolution.

Figure 10: Relative momentum resolution and transverse pointing resolution for disk investigations. The results are from the standard 7 disk setup, at $\eta = 3$, in a magnetic field of 1.5 T.

(a) Relative momentum resolution.

(b) Transverse pointing resolution.

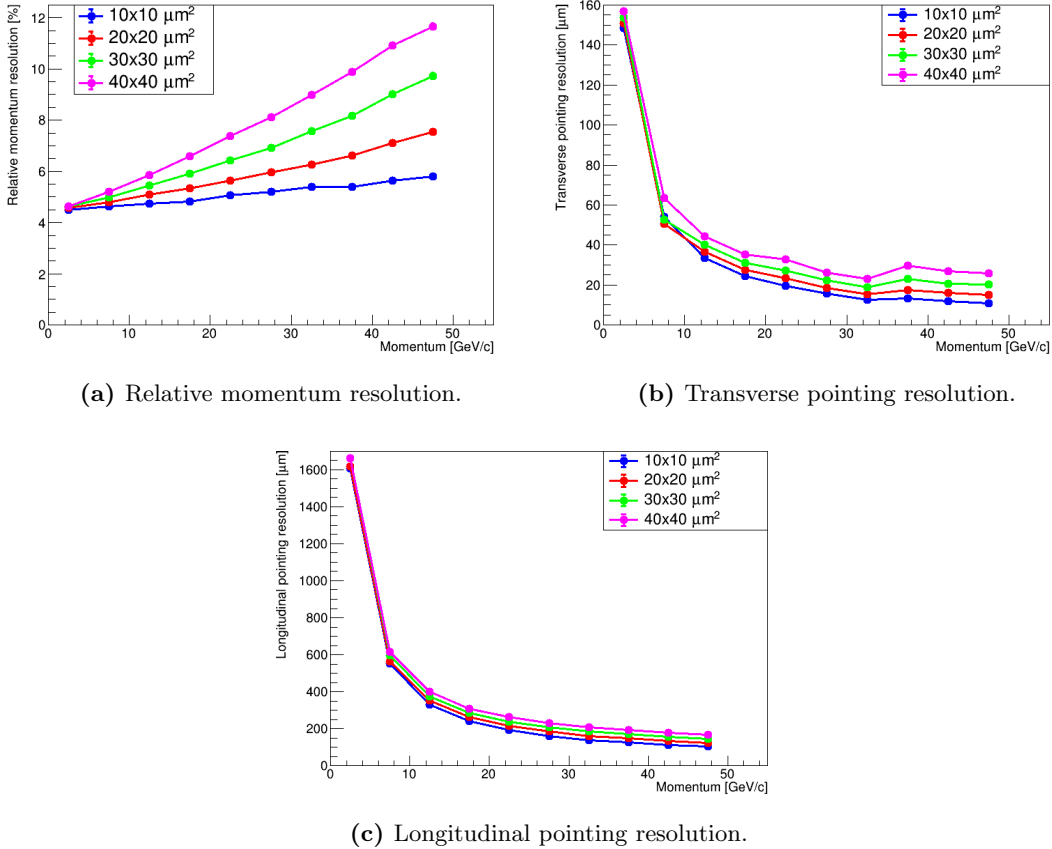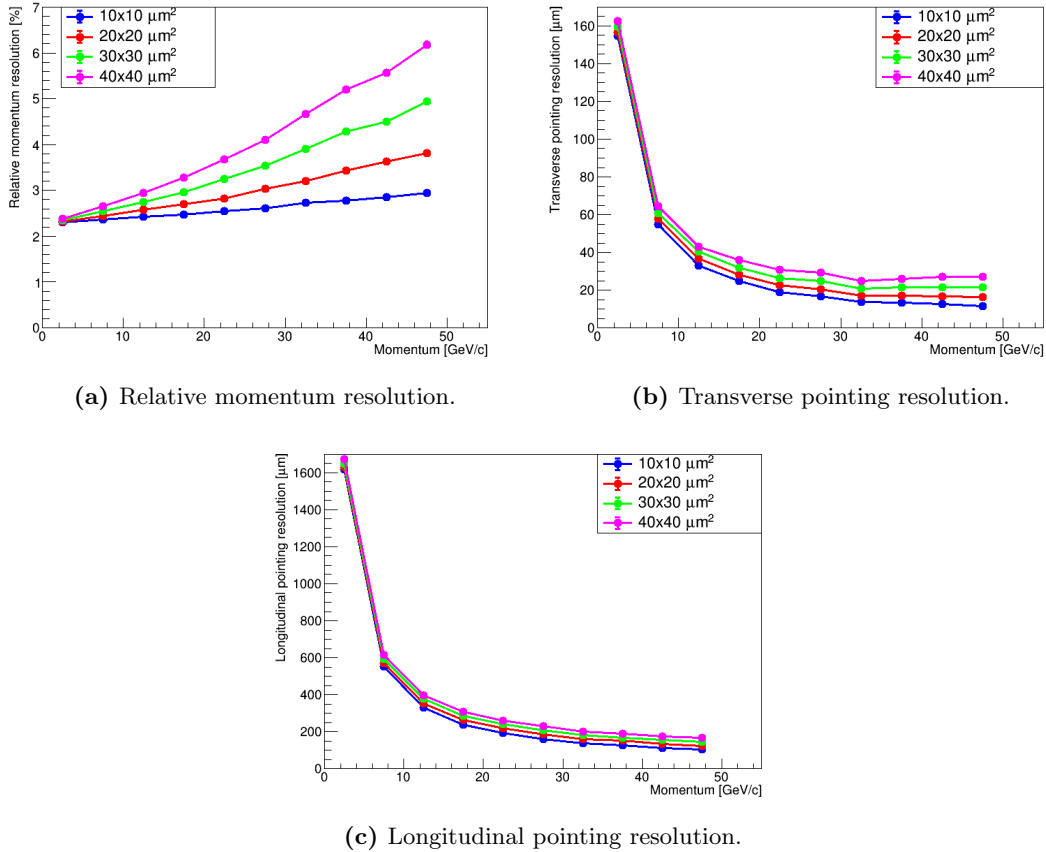(c) Longitudinal pointing resolution.

Figure 11: Relative momentum resolution and transverse pointing resolution for disk investigations. The results are from the standard 7 disk setup, at $\eta = 3$, in a magnetic field of 3 T.

The results once again show that a smaller pixel size improves all the resolutions, which is expected from theory. Since the momentum range is higher, there is more of a spread in the relative momentum resolution, as the geometric part of the theory dominates at higher momenta (see Equation A.20).

Comparing the results for the different magnetic field strengths, there is once again a close match with theory. The relative momentum resolution is inversely proportional to the magnetic field strength, and a factor of 2 difference can be seen in relative momentum resolution for the simulations. The pointing resolutions are largely unaffected by changing the magnetic field, again in agreement with theory.

The same simulation is also done for a setup with five disks, instead of seven. These simulations use the same parameters as before, but are only run for a magnetic field of 3 T. The five disks are placed equidistantly with the first one 250 mm from the centre point and the last one 1210 mm form the centre point. The results are shown in Figure 12.

These results are best compared to Figure 11, which is the 7 disk layout with a 3 T magnetic field. There is very little difference between a 7 disk layout and a 5 disk layout in this case. The relative momentum resolution for the 5 disk layout is slightly better, due to the decrease in material. The pointing resolutions show little to no change. This agrees with theory, where the innermost layer is most important for pointing resolution, and the length of the lever arm is the most important for momentum resolution. Neither of those two main parameters change between having 5 or 7 disks.

Comparing results to simulations performed by eRD16 [11], some discrepancies were found. After
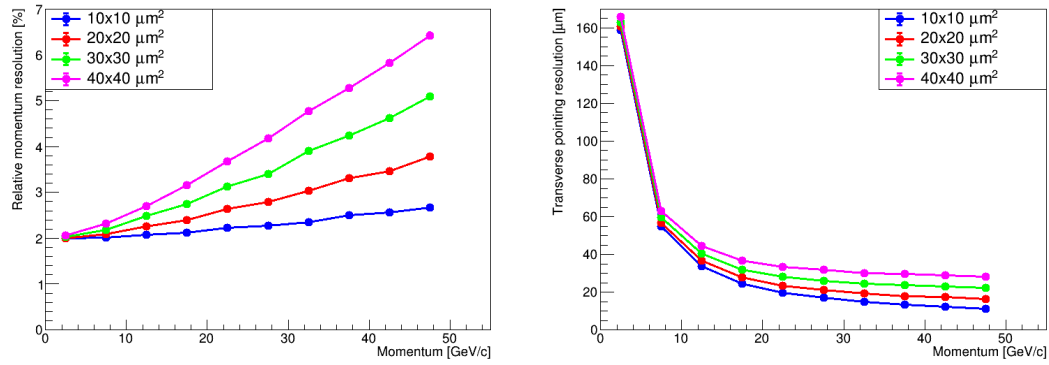
(a) Relative momentum resolution.

(b) Transverse pointing resolution.
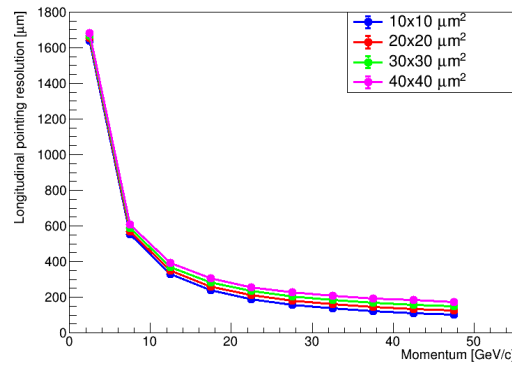
(c) Longitudinal pointing resolution.

Figure 12: Relative momentum resolution and transverse pointing resolution 3 T, 5 disks equally spaced between 250.0 mm and 1210.0 mm from centre point.

discussions, it was found that there were a few differences having the compound effect of making the results slightly different. One such difference was the magnetic field map used. There were also slight differences in analysis method. Details can be found in Appendix B. However, despite the minor discrepancies, the trends seen in the results are the same, indicating that the relative comparisons between different simulated layouts and pixel sizes are in agreement.

3.7   Innermost disk position

Using seven disks, simulations are made testing the effect of changing the innermost disk position. The innermost disk is placed at different distances from the centre point, whereas the outer 6 disks are kept in the same positions they are in in the previously described pixel size studies; i.e. equally spaced between 410 mm and 1210 mm from the centre point. Simulations are run for innermost disk distances from the centre point of 140 mm (5 mm from the inner barrel layers), 195 mm, 225 mm, 240 mm, 250 mm (which is the standard position, used in the pixel size studies), 275 mm, and 305 mm. The simulation parameters used are shown below.

- Particle: e^-

- Momentum range: 0 to 50 GeV/c (uniform in p)

- Pseudorapidity: $\eta = 3$

- No barrel and no TPC present

- Number of events: 500 000

- Pixel size: $20 \times 20 \ \mu m^2$

- Magnetic field: 3 T

The results of the simulations are shown in Figure 13.

(a) Relative momentum resolution.

(b) Transverse pointing resolution.

(c) Longitudinal pointing resolution.

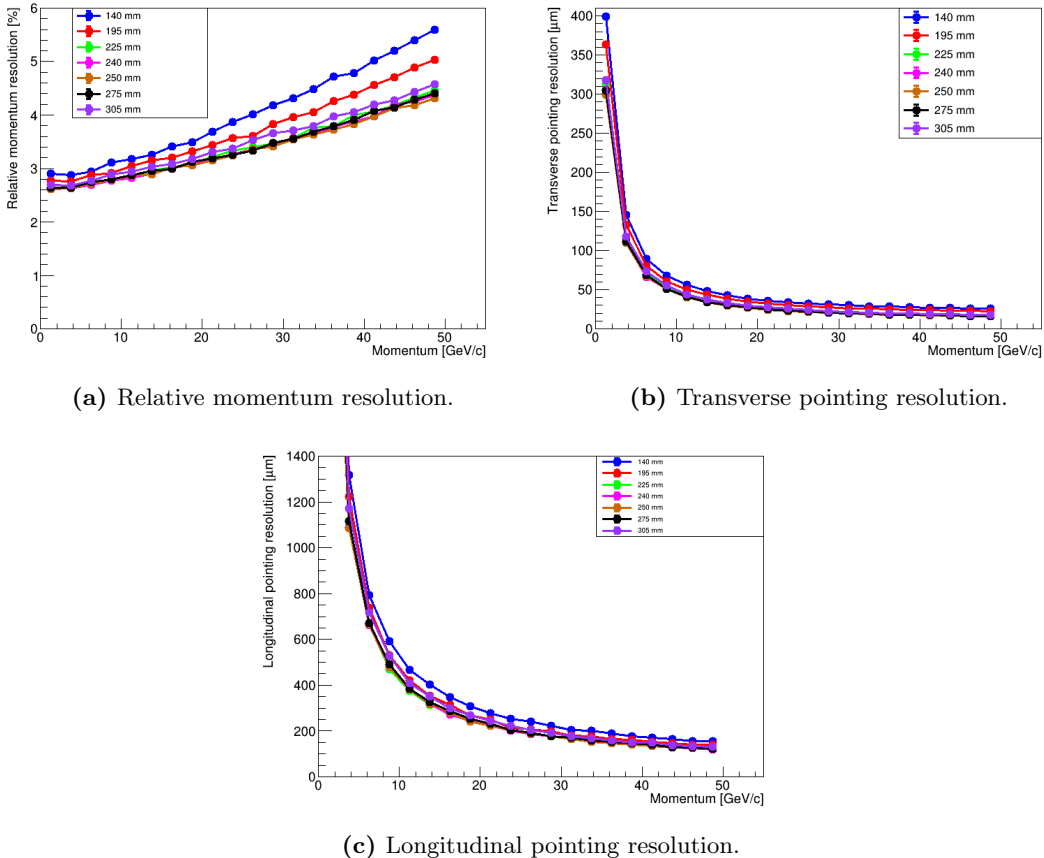**Figure 13:** Relative momentum resolution and pointing resolutions for a 7 disk layout, with varying innermost disk positions.

At first glance, the results seem to indicate a discrepancy with theory. The shortest distance (140 mm) appears to be the worst one, whereas theory suggests that having the innermost layer closer to the interaction point ought to make it better. However, looking at how the disks are

produced in simulations in conjunction with the disk positioning, this appears to be an effect of the disk inner radius. Table 1 shows the pseudorapidity for the inner radius edge for a selection of disk positions. From this table, it can be seen that for a disk position of 140 mm, a particle with

Disk position	η of inner radius
140 mm	2.75
195 mm	3.01
250 mm	3.33
305 mm	3.52

Table 1: Pseudorapidity location of the innermost disk inner radius, for different disk positions.

pseudorapidity 3 will completely pass through the hole in the centre of the disk. This explains why a disk position of 140 mm gives the worst pointing resolution in this instance; it completely removes the innermost disk as an active detector part for the simulated particles.

For a disk position of 195 mm the particles should always just hit the disk. Disks will however be built up of staggered rectangular staves of silicon, so the inner holes will thus not be completely circular, and the simulations reflect this. This means that the particles with pseudorapidity 3 will hit the innermost disk when they emerge with certain azimuthal angles, and not with others. As the full results of the simulations make up an average of all simulated events, this shows up as a worse average resolution than what would be expected if the innermost disk were always hit.

When the disk is hit, there are also some trends that can be observed. As the disk moves further away from the centre point the lever arm decreases, which deteriorates the relative momentum resolution. The first detector hit is also further away from the interaction point, deteriorating the spatial resolutions.

In conclusion, an innermost disk position of 250 mm from the centre is best for momentum resolution at higher momenta. The difference is however small between the positions where the disk is fully hit and close to the centre. As the disk moves further out, a deterioration can be seen. It is however worth reiterating that this is for the special case of $\eta = 3$. If the innermost disk is hit, theory indicates that having it closer to the centre would improve the resolutions.

3.8   Different inner barrel length, with disks

To study the impact of changing the interface region between barrel and disks, simulations are run in a range of pseudorapidities encompassing both. For these simulations the baseline used is the standard barrel with 7 disks and no time-stamping layer. The innermost disk is always placed 5 mm from the inner barrel edge, and the next disk is placed 5 mm outside the outer barrel edge. The remaining disks are placed equidistantly up to a distance of 1210 mm from the centre point. All simulation runs have the same beampipe and TPC. The parameters used in the simulations are shown below.

- Particle: e^-

- Momentum range: 0 to 50 GeV/c (uniform in p)

- Pseudorapidity range: $0 \leq \eta \leq 2.5$

- Number of events: 100 000

- Pixel size: 20×20 μm^2

- Magnetic field: 1.5 T

The length of the inner barrel is adjusted, moving the inner disk accordingly. Figure 14 shows a sketch of the situation where the inner barrel is 270 mm long. The results of this investigation, with resolutions plotted versus the momentum, are shown in Figure 15. In Figure 16, the resolutions plotted versus the pseudorapidity are shown.
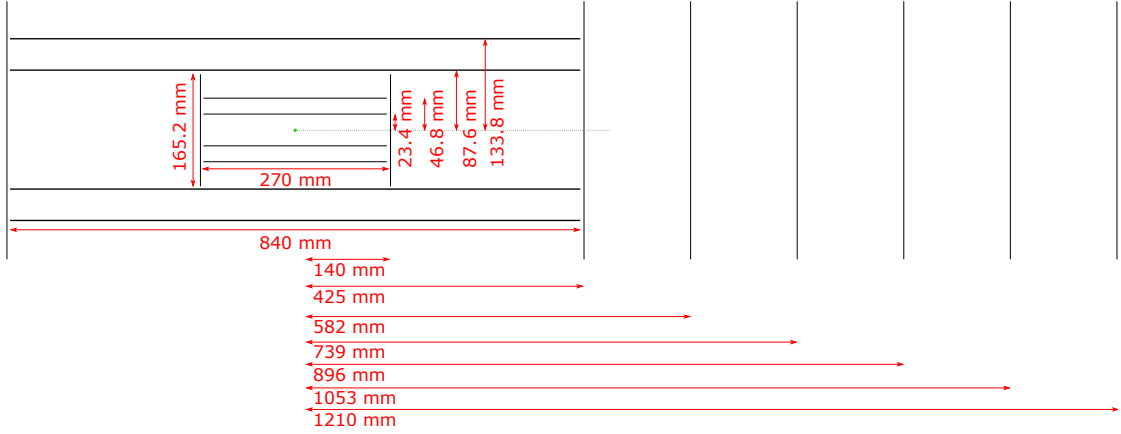
Figure 14: The layout of the detector, including disks. The inner barrel length is adjusted, and the innermost disk moves accordingly. The green dot indicates the centre point.
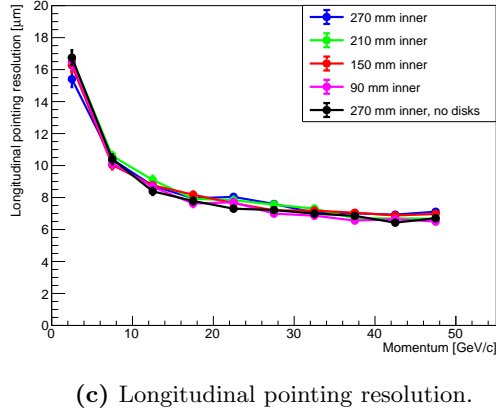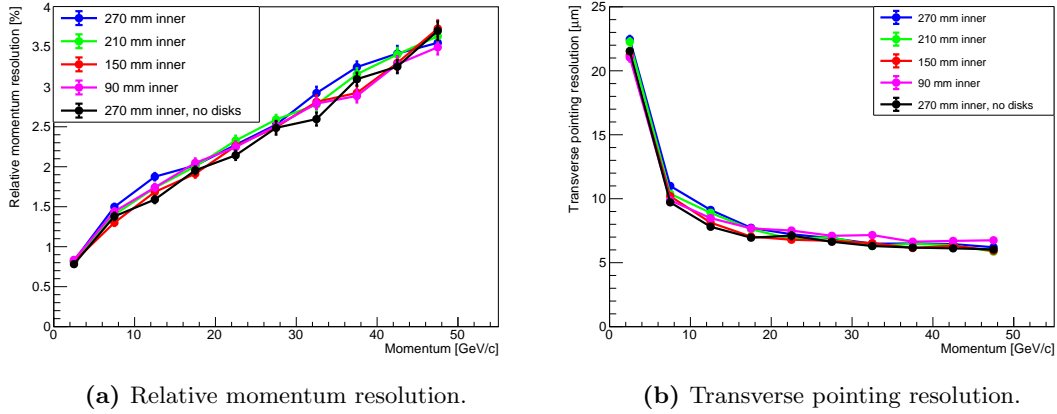

(a) Relative momentum resolution.

(b) Transverse pointing resolution.

(c) Longitudinal pointing resolution.

Figure 15: Relative momentum resolution and pointing resolutions versus momentum for different lengths of the inner barrel layers.

From Figure 15 it can be seen that in this situation, both the relative momentum resolution and the pointing resolutions are largely unaffected by the length of the inner barrel layers, for different values of the momentum p.

The insensitivity to the changes likely stems from the averaging over the investigated pseudorapidity range. For a given momentum, different events will have hit different regions of the detector. Some will thus be strongly affected by the placement of the disks and extent of the
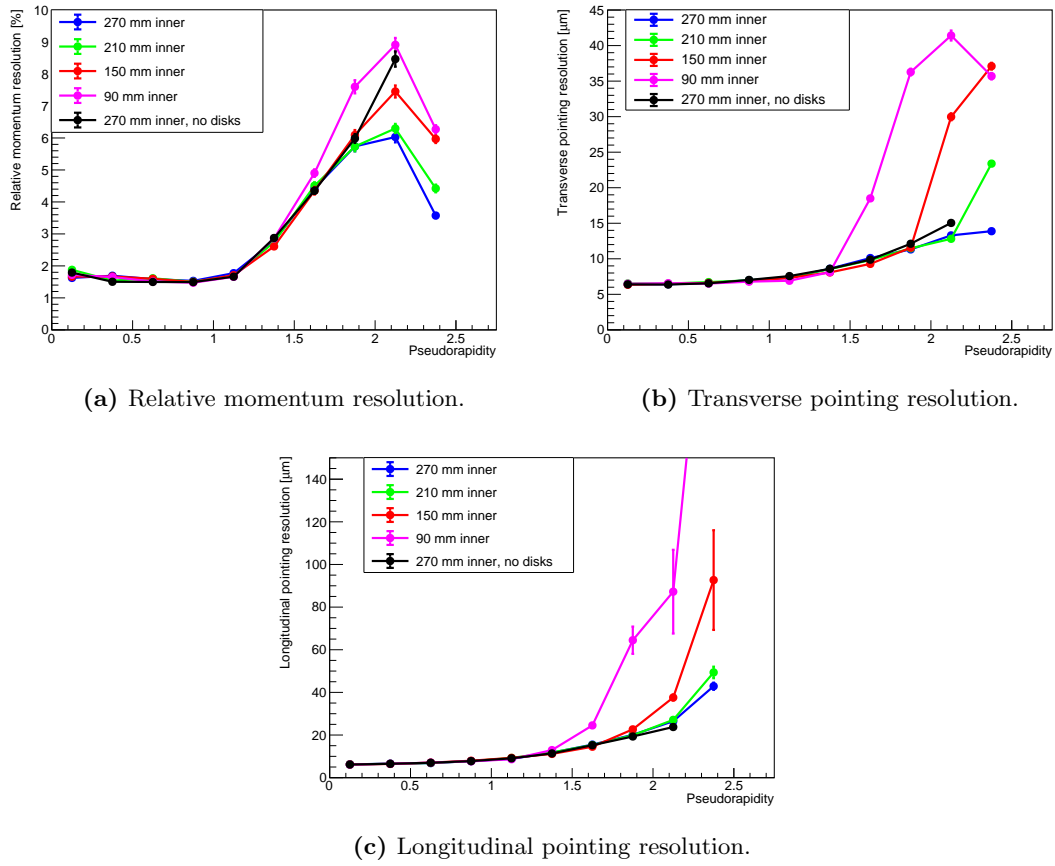
(a) Relative momentum resolution.

(b) Transverse pointing resolution.

(c) Longitudinal pointing resolution.

Figure 16: Relative momentum resolution and pointing resolutions versus pseudorapidity for different lengths of the inner barrel layers.

layers, whereas some will only be sensitive to the radii the barrel layers are placed at. In plots versus momentum, this will not show up explicitly other than as a small change of the full average resolution.

Figure 16 shows the same simulation results, plotted versus the pseudorapidity. Figure 17 shows a sketch of the detector with an inner barrel length of 270 mm, with pseudorapidities marked. The pseudorapidity coverage for the inner barrel layers and the first disk will change for shorter or longer inner barrels.
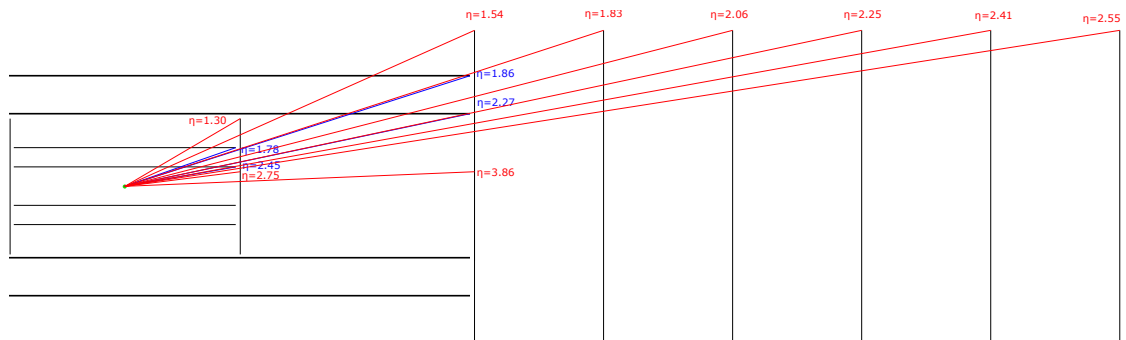

Figure 17: Detector sketch with pseudorapidities for different parts marked. The sketch is for an inner barrel length of 270 mm.

In the plots of resolutions versus pseudorapidity the effect of changing the layer length is clear. Looking first at the relative momentum resolution, it can be seen that it begins to deteriorate as the track length in the TPC gets shorter. The outer radius of the TPC is missed at $\eta \geq$ 1.06, which is where the curves start to turn upwards. At large pseudorapidities ($\eta \geq 2.1$) the resolution improves however, as the lever arm increases when more disks are hit. In the simulation containing no disks no parts of the detector are hit after a point, cutting the graph off.

In the pointing resolutions, there is a very clear deterioration as layers are missed. The big jump happens when the innermost layer is no longer hit, which makes sense as the innermost layer position is the main variable affecting the pointing resolution. For the 90 mm long inner layer particles also travel through the inner hole of the innermost disk at pseudorapidities larger than 1.65, and for the 150 mm long this happens at pseudorapidities larger than 2.13, thus missing the first disk as well as the innermost layer. When the disks are not present and the TPC is no longer hit, there are no more data points when the innermost layer is the only one hit as that is not enough for reconstruction.

3.9   Replacing gas TPC with silicon layers and disks

3.9.1   Different silicon layouts

In order to investigate the possibilities and potential benefits of an all-silicon tracker, simulations are made where the gas TPC is replaced with layers of silicon. Different layouts of this silicon replacement are tested, and results from the best basic layouts are combined into a final feasible design. In the simulations, the silicon vertex tracker barrel remains the same; the standard 4-layer barrel, with an added time-stamping layer. Seven disks are present in the forward region, at positions in z (along the beam axis) of 140.0 mm, 425.0 mm, 582.0 mm, 739.0 mm, 896.0 mm, 1053.0 mm, and 1210.0 mm. The radii of the disks are varied in the different layouts. The simulation parameters used are shown below. In the text that follows, the different layout names as presented in the resolution plots will be written in italics in parentheses.

- Particle: e^-
- Momentum range: 0 to 50 GeV/c (uniform in p)
- $0 \leq \eta \leq 2.5$
- Number of events: 100 000
- Pixel size: $20 \times 20 \ \mu m^2$
- Magnetic field: 1.5 T

First of all a reference run is made using the standard TPC (*With gas TPC*) with the regular basic disks. This is the layout shown in Figure 2. The first gas TPC replacement layout investigated keeps the standard disks, and replaces the gas TPC with four silicon layers (*2+2 layers, long*) with a thickness of 0.8 % X_0 each and a length of 1960 mm, which is the same length as the gas TPC. The first silicon layer is placed at a radius of 225.0 mm, which is the same as the innermost TPC radius. The second layer is placed as closely as possible to this, 46.2 mm further out (i.e. at a radius of 271.2 mm). Having two layers close together will help in finding the direction a particle travels, if it hits both layers. The final two layers in this layout are placed at radii of 728.8 mm and 775.0 mm, which is the gas TPC outer radius. A sketch of the layout can be seen in Figure 18. Detector staves this long may in reality require a slightly higher material thickness, but 0.8 % X_0 is used as an approximation in the simulations.

Tests are also done with a smaller radius replacement (*2 layers, long, small radius*), where the gas TPC is replaced by two silicon layers, at radii of 383.8 mm and 430.0 mm, and lengths of 1960 mm. This layout keeps the standard disks with their normal radii. A layout with shorter layers (840.0 mm long) is also tested at this radius (*2 layers, short, small radius; large disks*). This layout has enlarged disks, with a radius of 430.0 mm. The innermost disk radius is always kept the same, in order to fit inside the outer barrel layers.
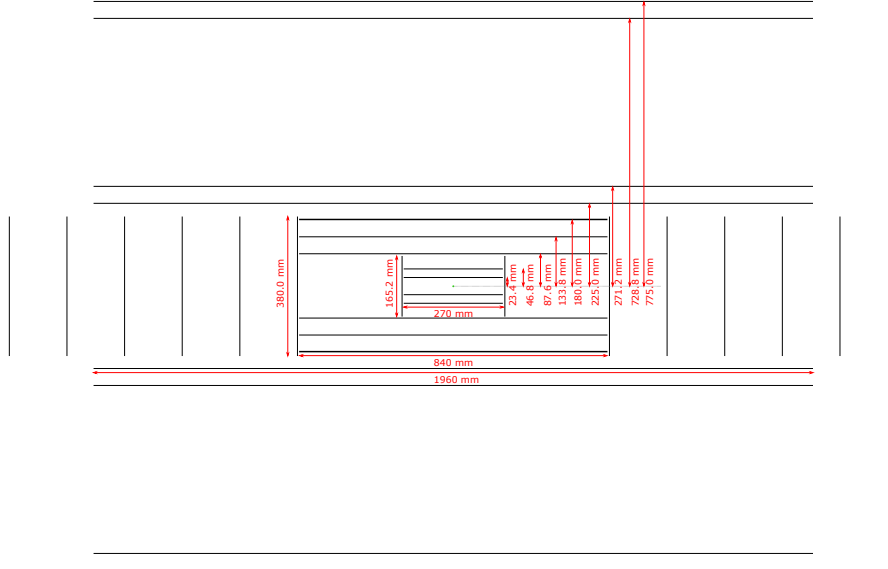
Figure 18: Sketch of the simulated layout with standard disks, where the gas TPC is replaced by two inner and two outer silicon layers.

The studies of the layouts with a smaller radius shows that larger disks improve momentum resolution in the investigated parameter space. More studies are therefore made with shorter layers (840.0 mm, the same length as the barrel outer layers) and larger disks. The full radius of 775.0 mm is used, and five silicon layers are used to replace the gas TPC. The layers are placed equidistantly between 225.0 mm and 775.0 mm. Five layers are used as a balance of tracking capability (which increases with number of detector hits) and material thickness. Tests are made with enlarged disks, with a radius of 420.0 mm (*5 layers, short; large disks*), and an optimised disk layout. The radius of 420.0 mm is used as that will give a maximum length across the disk of 840.0 mm; the same length as an outer barrel layer. The optimised disk layout is a combination of smaller disks and larger rings, combining the best-performing elements while keeping a realistic configuration (*5 layers, short; optimised disks*). The sizes of the disks and rings can be trimmed to give close to full silicon detector coverage in central to forward pseudorapidities. The optimised disks offer many possibilities of fine-tuning coverage in certain pseudorapidity regions. A sketch of this layout can be seen in Figure 19.

The layouts presented here are the key results from the investigation. Some of the other studied layouts, and the reasons they are not part of the main results, can be found in Appendix C.

Resolutions from the simulations are shown in Figure 20 versus momentum, and in Figure 21 versus pseudorapidity. From the plots, it can first of all be seen that the longitudinal pointing resolution is not significantly altered by changes in the TPC region. With disks of the same thickness, position, and pixel size in place, there is never much difference.

Looking at the relative momentum resolution versus momentum, it is first noteworthy that above momenta of around 5 GeV/c, some of the silicon configurations outperform the gas TPC. This is likely to a large extent due to the much smaller pixel size of the silicon layers, giving a better intrinsic resolution compared to the TPC. Only the long small radius layout with standard disks (*2 layers, long, small radius*) does not outperform the gas TPC at any point. This is due to the decrease in lever arm length, which strongly affects the relative momentum resolution. Decreasing the length and making room for a larger disk size improves the momentum resolution, as seen by comparing the two different small radius layout results (i.e. the curves labelled *2 layers, long, small radius* and *2 layers; short, small radius; large disks*).

In the plot of transverse pointing resolution versus momentum, there is no significant difference between any of the layouts. This is expected, since the innermost layers of the detector do not change.
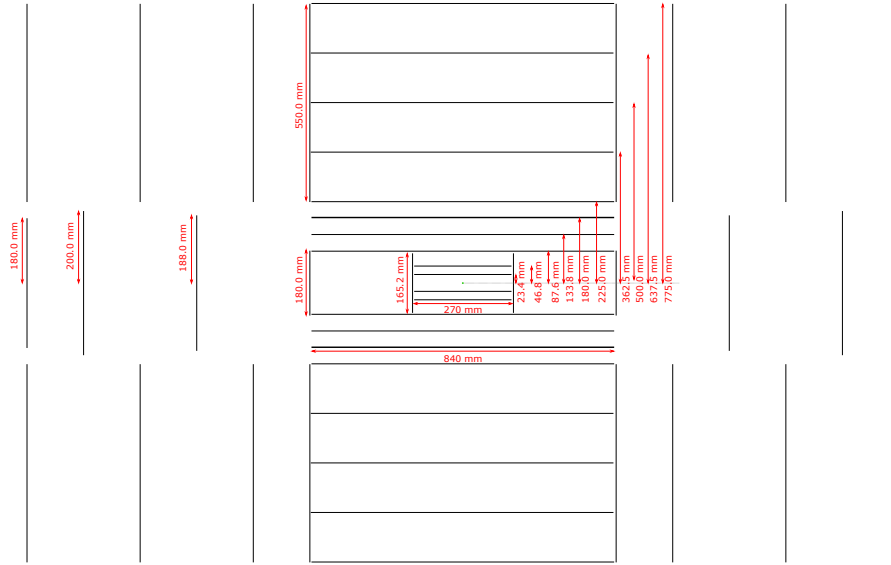
Figure 19: Sketch of the simulated layout with optimised disks, where the gas TPC is replaced by five equidistant silicon layers, as well as disks and rings to give pseudorapidity coverage in the forward and backward regions.

(a) Relative momentum resolution.

(b) Transverse pointing resolution.

(c) Longitudinal pointing resolution.

Figure 20: Relative momentum resolution and pointing resolutions versus momentum for different gas TPC replacement configurations.

(a) Relative momentum resolution.

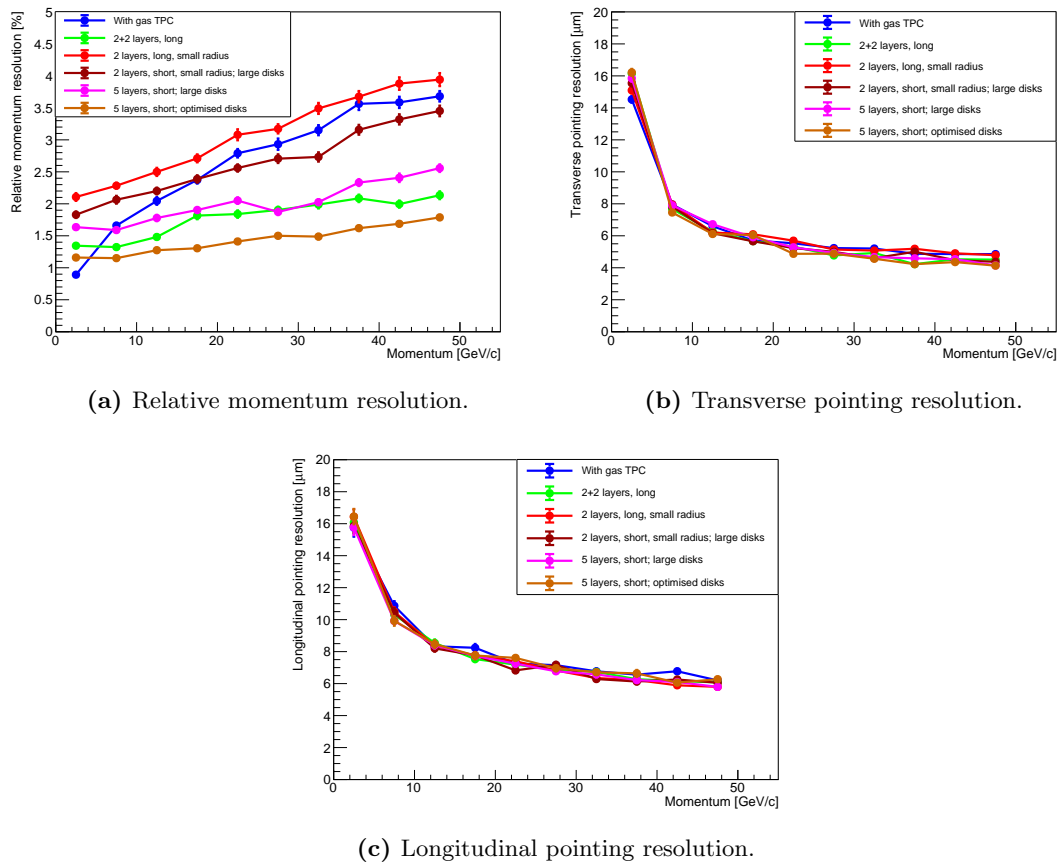(b) Transverse pointing resolution.

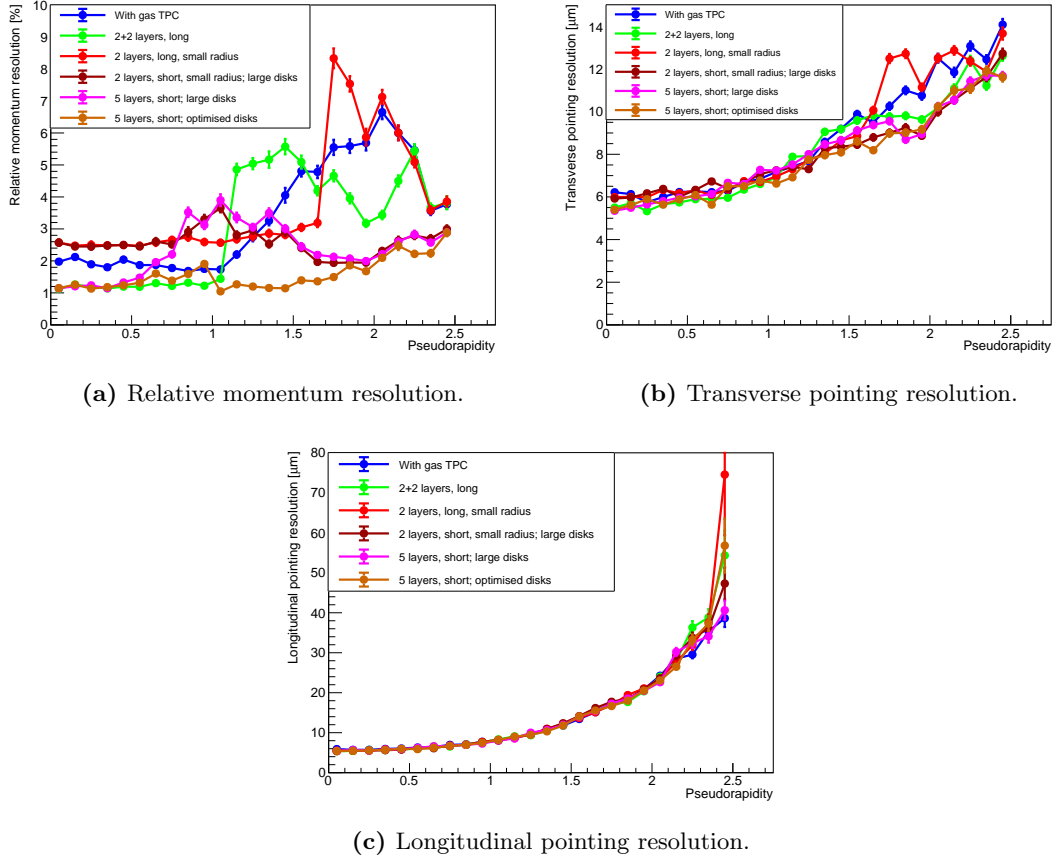(c) Longitudinal pointing resolution.

Figure 21: Relative momentum resolution and pointing resolutions versus pseudorapidity for different gas TPC replacement configurations.

Looking at the plot of relative momentum resolution versus pseudorapidity, more details of where the momentum resolution losses come from for the different layouts can be seen. The resolution of the gas TPC layout starts to deteriorate as the path length through the gas decreases. It then improves again once more disks are hit, at pseudorapidities $\eta \geq 2.1$. The layout with two inner and two outer silicon layers (*2+2 layers, long*) immediately loses momentum resolution when the outer two layers are no longer hit, at $\eta \geq 1.1$. Like the gas TPC layout, resolution is then improved again once disks are hit and the lever arm increases. In a pseudorapidity interval of $1.1 \leq \eta \leq 2.3$ however, the relative momentum resolution for this layout is much worse than it is at central pseudorapidities.

The momentum resolutions of the small radius layouts follow each other well at $\eta \leq 1.5$. After this however, it becomes apparent that having shorter layers and larger disks improves momentum resolution.

Comparing the five layer layouts, their momentum resolutions are the same at $\eta \leq 0.5$. After that however, they diverge in the interval $0.5 < \eta \leq 1.9$, with the optimised disk layout having better resolution consistently. This is due to the detector gaps in pseudorapidity present in the 420 mm (large) disk layout, where layers are missed. These gaps are closed by disks and rings in the optimised disk layout.

Looking at the transverse pointing resolution versus pseudorapidity, most layouts have no significant difference. Only the long small radius layout with standard disks and the gas TPC layout are worse than the others, at $\eta \geq 1.6$.

In conclusion, the layout with disks and rings, that combines the best parts of the other tested

layouts into a physically viable construction, outperforms the gas TPC in all the studied parameter space, apart from at momenta below 4 GeV/c.

The ridges seen in the plots versus pseudorapidity have a direct correspondence to gaps in the detector coverage. Fine-tuning the layout can minimise the gaps and improve the resolutions. This can be done effectively for any of the proposed detector concepts for the EIC.

Important to note in this study is that a gas TPC gives many points through which a track can easily be extrapolated, whereas a few silicon layers can make unambiguous reconstruction more difficult in a more realistic test (e.g. full event reconstruction, rather than single particle). One solution would be to increase the number of silicon layers, while keeping in mind that an increased material thickness deteriorates resolution. The smaller pixel size possible with the silicon is also beneficial for the reconstruction however, so a balance can likely be reached between performance and material thickness. The five layer layout is an attempt at reaching this balance. In a study made comparing two silicon layers to five, it is found that having five silicon layers instead of two is not severely detrimental to any of the resolutions in this parameter space. Details of this study can be found in Appendix C. A gas TPC can also help with particle identification. This would need to be handled by other detectors, if an all-silicon tracker layout is used.

Comparing the two different five layer layouts, it can clearly be seen that the optimised disk layout has better relative momentum resolution than the 420 mm disk layout. In the plot versus momentum, there is always a difference of approximately 0.5 % between them, with the optimised disk layout being lower. In the plot versus pseudorapidity, the relative momentum resolution of the 420 mm disk layout is up to 2 % higher than the optimised disk layout at certain pseudorapidities, and never lower. In the following studies, only the optimised disk layout will thus be considered.

3.9.2 Different silicon replacement outer radius

Using silicon layers instead of a gas TPC can potentially make it possible to reduce the overall tracker radius without severe loss of performance. Dedicated studies are therefore made for different outer radii of the detector, utilising the results from Section 3.9.1. The best-performing silicon configuration, shown in Figure 19, is simulated for different outer radii, keeping the five silicon layers equidistantly spaced between a radius of 225.0 mm and the currently investigated maximum outer radius. The minimum distance between layers is 46.2 mm, resulting in a smallest possible outer radius of 409.8 mm. Outer radii of 500.0 mm, 600.0 mm, and 775.0 mm (which is the standard radius as presented in Figure 19) are also tested. The radius of the rings is changed to match the currently investigated outer radius, in order to keep the full tracker radius at the investigated level. The 420 mm radius disk layout described in Section 3.9.1 is also investigated in this way, and results from this can be found in Appendix C.

Studies are made both in the central region and in the forward region, with slightly different parameters. For the central regions, the following parameters are used:

- Particle: e^-
- Momentum ranges: 0 to 5 GeV/c and 0 to 30 GeV/c
- Pseudorapidity ranges: $-1 \leq \eta \leq 1$ and $0 \leq \eta \leq 1$
- Number of events: 100 000
- 5 layer barrel (two inner, two outer, one time-stamping layer)
- Pixel size: $20{\times}20$ μm^2
- Magnetic field: 1.5 T

There is no significant difference in any of the pointing resolutions in this study, so only the relative momentum resolution results are shown. The gas TPC layout used is the standard one, with an outer radius of 775.0 mm, as shown in Figure 2. Figure 22 shows the relative momentum resolution versus momentum and pseudorapidity in the momentum interval 0 to 5 GeV/c and

pseudorapidity interval $-1 \leq \eta \leq 1$. In Figure 23, the same can be seen for the study performed in the momentum interval 0 to 30 GeV/c and pseudorapidity interval $0 \leq \eta \leq 1$.

The study of momenta between 0 and 5 GeV/c is made in order to observe the differences for very low momenta, whereas the 0 to 30 GeV/c study is made to investigate the detector performance at the most probable electron momenta in the central region [8].
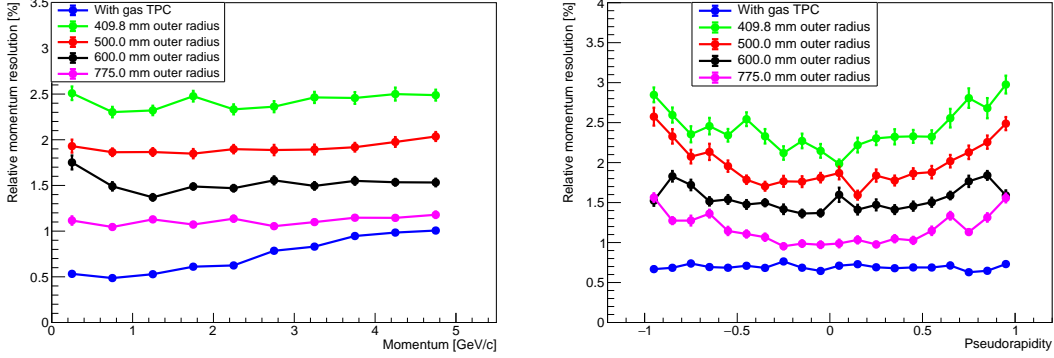
(a) Relative momentum resolution versus momentum.

(b) Relative momentum resolution versus pseudorapidity.

Figure 22: Relative momentum resolution versus momentum and pseudorapidity for different silicon TPC replacement outer radii, in the momentum range 0 to 5 GeV/c and pseudorapidity range $-1 \leq \eta \leq 1$.
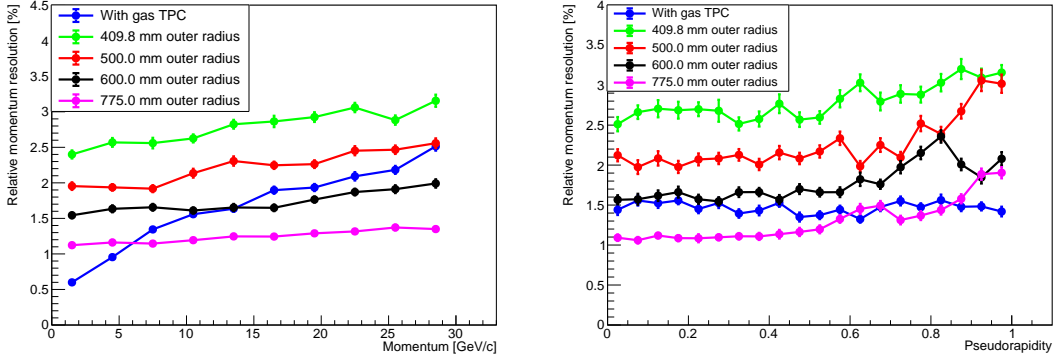
(a) Relative momentum resolution versus momentum.

(b) Relative momentum resolution versus pseudorapidity.

Figure 23: Relative momentum resolution versus momentum and pseudorapidity for different silicon TPC replacement outer radii, in the momentum range 0 to 30 GeV/c and pseudorapidity range $0 \leq \eta \leq 1$.

At all momenta below 5 GeV/c, the gas TPC outperforms the silicon replacement in relative momentum resolution at all pseudorapidities between -1 and 1. The largest difference when comparing to the smallest silicon replacement (with an outer radius of 409.8 mm) to the 775.0 mm gas TPC is 2 %. At momenta approaching 5 GeV/c, the difference between the gas TPC and the silicon replacements decreases.

Looking at the higher momentum interval (0 to 30 GeV/c), it can be seen that the gas TPC loses performance faster with increasing momentum than the silicon layouts do. The points where the different silicon layouts start having better relative momentum resolutions than the gas TPC can be seen. The 775.0 mm outer radius silicon layout is better at momenta above 6 GeV/c. The

600.0 mm silicon layout is equally good or better at momenta above approximately 11 GeV/c. The 500.0 mm is equally good at 30 GeV/c. For the 409.8 mm radius silicon layout, the difference to the gas TPC decreases from 2 % at low momenta to approximately 0.5 % at 30 GeV/c, but it never outperforms the 775.0 mm radius gas TPC.

Looking at the pseudorapidities, the 775.0 mm silicon layout is equal to or outperforms the gas TPC at $\eta \leq 0.9$. The 600.0 mm silicon layout matches the performance of the gas TPC at $\eta \leq 0.5$. The smaller radius layouts are always 0.5 % to 1.5 % worse in relative momentum resolution than the gas TPC in this parameter space.

Note again that for momenta below 5 GeV/c, the gas TPC has better relative momentum resolution than any of the investigated silicon layouts.

The same study is performed in the forward region, using the following parameters;

- Particle: e^-
- Momentum range: 0 to 50 GeV/c
- Pseudorapidity range: $1.0 \leq \eta \leq 2.5$
- Number of events: 100 000
- 5 layer barrel (two inner, two outer, one time-stamping layer)
- Pixel size: $20 \times 20 \ \mu\mathrm{m}^2$
- Magnetic field: 1.5 T

In this study the longitudinal pointing resolution never differs significantly and is not shown. Figures 24 and 25 show the resolutions for different radii of the optimised disk layout versus momentum and pseudorapidity, respectively.
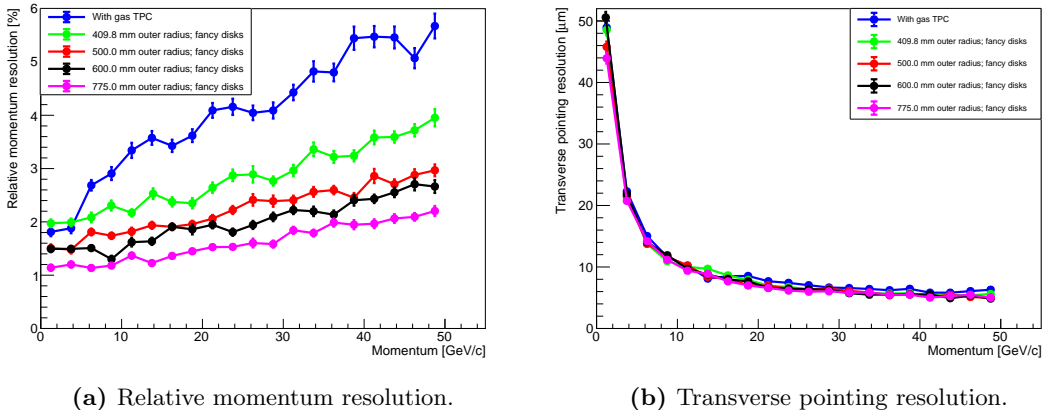

(a) Relative momentum resolution.   **(b)** Transverse pointing resolution.

Figure 24: Relative momentum resolution and transverse pointing resolution versus momentum for different silicon TPC replacement outer radii, with optimised disk layout. Forward regions $(1 \leq \eta \leq 2.5)$.

Looking at Figure 24, it can be seen that the optimised disk layout has better relative momentum resolution than the gas TPC at all momenta when the radius is 500.0 mm or larger. The layout with an outer radius of 409.8 mm only outperforms the gas TPC at momenta exceeding 5 GeV/c. The 775.0 mm outer radius is the best layout tested, but the difference in relative momentum resolution to the 500.0 mm layout is at most slightly less than 1 %. The difference in transverse pointing resolution is small for all tested layouts.

In Figure 25, it can first of all be seen that for transverse pointing resolution, the gas TPC is worse than any radius of silicon for pseudorapidities between approximately 1.5 and 2.3. For the
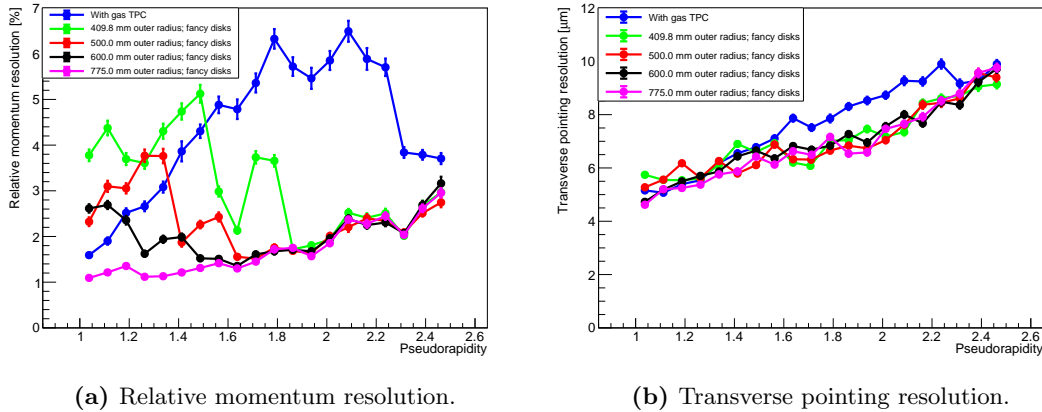
(a) Relative momentum resolution.

(b) Transverse pointing resolution.

Figure 25: Relative momentum resolution and transverse pointing resolution versus pseudorapidity for different silicon TPC replacement outer radii, with optimised disk layout. Forward regions ($1 \leq \eta \leq 2.5$).

relative momentum resolution, the silicon layouts are different up until a pseudorapidity of 1.9, whereafter they are the same (as is expected, since the layouts are identical in this region of the disks). The 775.0 mm outer radius layout always has better relative momentum resolution than the gas TPC in the investigated parameter space. The 600.0 mm layout has better momentum resolution than the gas TPC at $\eta \geq 1.2$, and the 500.0 mm layout has better resolution at $\eta \geq 1.4$. The 409.8 mm silicon layout outperforms the gas TPC at pseudorapidities larger than 1.55. The gas TPC relative momentum resolution is at most 2.5 % lower than the 409.8 mm silicon layout relative momentum resolution.

To investigate at what radius silicon outperforms a gas TPC, different outer radii of the gas TPC are studied in the central region, and compared to the previously discussed all-silicon simulations with five silicon layers replacing the gas TPC. The parameters used are listed below.

- Particle: e^-
- Momentum range: 0 to 30 GeV/c
- Pseudorapidity range: $0 \leq \eta \leq 1$
- Number of events: 100 000
- 5 layer barrel (two inner, two outer, one time-stamping layer)
- Pixel size: $20 \times 20 \ \mu m^2$
- Magnetic field: 1.5 T

The radii tested mimic those of the silicon replacement layouts; 409.8 mm, 500.0 mm, 600.0 mm, and (the standard gas TPC outer radius) 775.0 mm. The results are compared to the simulations performed with the optimised disks layout.

Figure 26 shows the gas TPC (blue) superimposed on the 775.0 mm radius silicon replacement layout (green). The range of pseudorapidities between -1 and 1 are marked by purple dashed lines.

The resolutions resulting from these simulations can be seen in Figure 27 versus momentum, and in Figure 28 versus pseudorapidity. The longitudinal pointing resolution does not change significantly between the different layouts, and is thus not shown. In the figures, the colours match radii. A solid line with circular markers indicates that the data correspond to a silicon layout, and a dashed line with square markers indicates a gas TPC of the same radius.
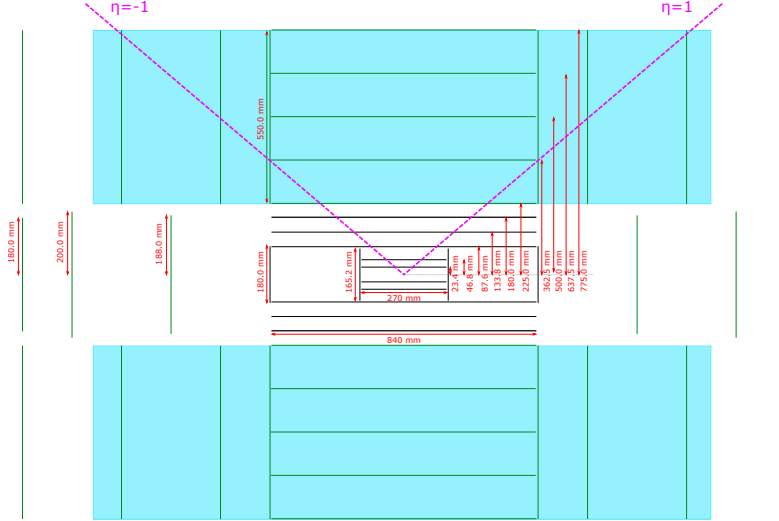
Figure 26: Sketch of the gas TPC (blue) superimposed on the 775.0 mm radius silicon replacement layout (green). The dashed lines indicate $|\eta| = 1$.

(a) Relative momentum resolution.

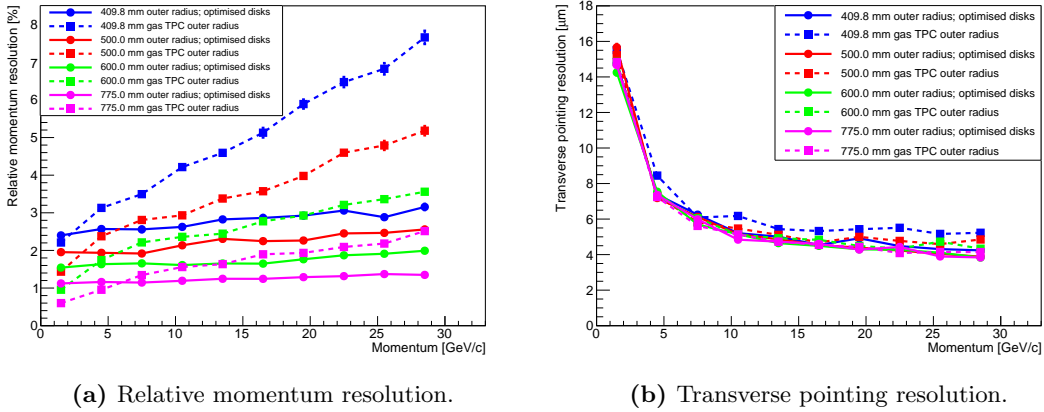(b) Transverse pointing resolution.

Figure 27: Relative momentum resolution and transverse pointing resolution versus momentum, comparing 5 layer silicon replacement with gas TPC for different maximum outer radii.

From the plot of transverse pointing resolution versus momentum, it can be noted that the transverse pointing resolution for a small-radius gas TPC is worse than the other tested layouts at most momenta. This is likely due to the decrease in lever arm, in combination with the relatively poor spatial resolution of the gas TPC (compared to silicon).

Looking at the relative momentum resolution versus momentum plot, it can be seen that silicon is always equal to or better than a gas TPC if they both have a maximum radius of 409.8 mm. In all cases, the relative momentum resolution for the silicon layout deteriorates slower with increasing momentum than it does for the gas TPC. The silicon layouts are thus always better than the gas TPC at high momenta. The location of the crossover point where silicon becomes better than gas depends on the radius. For the 500.0 mm radius, the gas TPC is better at momenta below 3 GeV/c. For the 600.0 mm radius, the gas TPC is better at momenta below approximately 4 GeV/c. At a radius of 775.0 mm, the gas TPC has a better relative momentum resolution at momenta below 6 GeV/c.

The transverse pointing resolution versus pseudorapidity plot in Figure 28 shows that the gas TPC at 409.8 mm radius has the worst pointing resolution in the whole investigated pseudorapidity range ($0 \leq \eta \leq 1$). In general the silicon layouts are shown to have the best transverse
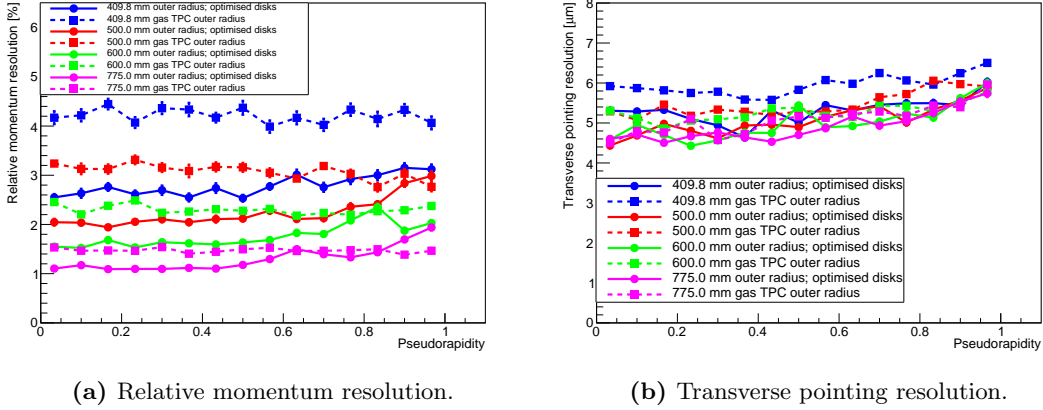
(a) Relative momentum resolution.

(b) Transverse pointing resolution.

Figure 28: Relative momentum resolution and transverse pointing resolution versus pseudorapidity, comparing 5 layer silicon replacement with gas TPC for different maximum outer radii.

pointing resolution here, but the difference between silicon and gas for each radius is below 1 μm.

Looking at the relative momentum resolution versus pseudorapidity, it can immediately be seen that the silicon layouts at 409.8 mm radius and 500.0 mm radius are better than their gas TPC counterparts across the full range investigated. The 500.0 mm radius silicon layout also outperforms or matches the 600.0 mm radius gas TPC at pseudorapidities smaller than 0.8. The silicon layout with radius 600.0 mm always outperforms or matches the 600.0 mm radius gas TPC. Finally, the 775.0 mm radius silicon layout has better or equal relative momentum resolution than the standard gas TPC at pseudorapidities below 0.85. In general, the difference between silicon layouts and gas TPC increases as the radius decreases, in favour of the silicon layout. In the investigated parameter space, an all-silicon layout has better performance than a gas TPC as soon as the radius is decreased from the baseline of 775.0 mm. In other words, if it is decided that the tracker radius is to be decreased from 775.0 mm, an all-silicon layout is preferable to a gas TPC.

4   Conclusions and outlook

In conclusion, the best silicon vertex tracker layout indicated by the performed simulations is one with two inner layers (two are needed to keep redundancy, and improves pointing resolution at higher momenta), two outer layers, and disks in the forward and backward regions. Having two outer layers instead of just one makes little difference, but an extra layer may help in getting an accurate particle track for vertex reconstruction. A time-stamping layer does not have a severe negative impact on any of the resolutions, but can aid the detection in other ways. The detector benefits from keeping the pixel size in all layers as small as possible, and the optimal pixel size is currently considered to be 20×20 μm^2.

The simulations indicate that for particles with momenta above around 5 GeV/c, the resolutions can benefit from replacing the gas TPC with silicon layers. The best silicon vertex tracker, as shown by the simulations, will thus be something similar to the sketch shown in Figure 19. This is a baseline layout that can be adapted to any of the suggested detector concepts with small alterations to accommodate different beampipes and fit in with other detector parts. If the detector is to be more compact than the baseline radius of 775.0 mm, the simulations indicate that it is beneficial to replace the gas TPC with layers of silicon and larger disks and rings.

In EICROOT, there are limited things that can still be done. Currently different simulation frameworks are investigated, with the goal of inputting Pythia events and doing reconstruction of physics observables. This would make it possible to investigate detector characteristics under conditions more similar to the real experiment. The focus will be on reconstructing charmed mesons, such as the D^{*+} and D^0. First of all however, the simulation frameworks will be benchmarked with similar simulations as the ones described in this document and compared to the EICROOT results.

A   Theoretical background

A.1   Particle interactions

A.1.1   Radiation length

Radiation length is a quantity used to describe how far radiation penetrates through a material. It is defined by the energy lost due to bremsstrahlung of an electron (or positron) travelling through the material.

Bremsstrahlung occurs when the incoming charged particle interacts with the electric fields of the atomic nuclei in the traversed material. For relativistic electrons, the energy loss per length is given by [12]

$$\frac{dE}{dx} = -\frac{E(x)}{X_0},$$
(A.1)

where X_0 is the radiation length. Integrating this, the energy as a function of distance travelled by the electron is given by

$$E(x) = E_0 \cdot e^{-x/X_0}.$$
(A.2)

E_0 is the initial total energy of the electron. The radiation length X_0 is thus defined as the distance over which the energy of an electron is reduced by a factor of $1/e$ due to bremsstrahlung.

Radiation length is a material property, and can be calculated from material constants. An approximation is given by [13]

$$X_0 = \frac{1}{\rho} \frac{716.4 \text{ g/cm}^2 \cdot A}{Z(Z+1) \cdot \ln\left(287/\sqrt{Z}\right)},$$
(A.3)

where ρ is the material density (in g/cm^3), A is the mass number of the material, and Z its atomic number. With these units, Equation A.3 gives the radiation length in centimetres.

The radiation length thus depends on both Z and Z^2. The Z^2 dependence comes from elastic scattering between the electron and the nucleus, and the Z dependence comes from elastic scattering between the incoming electron and the atomic electrons [13].

Radiation length is a useful tool for characterising the thickness of a detector, and detector material thickness is commonly expressed in percentages of radiation length.

A.1.2   Multiple scattering

Charged particles traversing media scatter multiple times due mainly to interactions with the Coulomb fields of atomic nuclei in the media. This is known as multiple scattering, or multiple Coulomb scattering. The full distribution of scattering angles is well described by Molière's theory of multiple scattering [14]; for small angles of deflection the distribution is approximately Gaussian, but for larger angles it more resembles Rutherford scattering, with larger tails than a Gaussian distribution. Most of the deflections caused by the scattering result in small angular deflections of the incident particle, and thus the Gaussian distribution approximation can be used in most cases. With this approximation, the distribution of the total scattering angle θ relative to the incidence direction is given by [13]

$$f(\theta) = \frac{1}{\sqrt{2\pi} \cdot \sigma_\theta} \cdot e^{-\theta^2/2\sigma_\theta}.$$
(A.4)

It is thus a Gaussian distribution centred around 0°, with standard deviation σ_θ. The standard deviation of the Gaussian distribution for multiple scattering is given by the "Highland formula" as [15, 16]

$$\sigma_\theta = \frac{13.6 \text{ MeV/c}}{p \cdot \beta} \sqrt{\frac{x}{X_0}} \left(1 + 0.038 \cdot \ln\left(\frac{x}{X_0}\right)\right).$$
(A.5)

Here p is the momentum of the incident particle, $\beta = v/c$ its velocity (expressed as a fraction of the speed of light), x is the length of scattering material traversed by the particle, and X_0 is the radiation length of the material. For small values of x/X_0, which is the case in tracking detectors, Equation A.5 can be approximated as

$$\sigma_\theta \simeq \frac{13.6 \text{ MeV/c}}{p \cdot \beta} \sqrt{\frac{x}{X_0}}. \tag{A.6}$$

From this it can be seen that the distribution of angles gets wider for lower particle momenta and velocities. Hence the particle trajectory is more likely to be more deflected for lower energy particles traversing a detector, reducing the possible accuracy of position measurements. This also shows the importance of keeping the material budget of detectors low, as a thicker detector or a lower radiation length in it will increase x/X_0, increasing the probability for a larger multiple scattering angle and thus the uncertainty in measuring track position.

A.2 Detector properties

A.2.1 Spatial resolution of segmented detector

The spatial resolution in one direction of a detector segment is mainly determined by the size of the segment, and the charge sharing between segments. Making the approximations that charge sharing is not present, that the readout is binary (i.e. that a particle is either detected or not; there is no signal amplitude information), and that the detector is uniform and fully efficient across the entire segments, the spatial resolution as a function of segment size can be determined.

Assuming that the segment reaches between points a and b, an incoming particle will be detected with uniform probability if it hits between the two points, and not at all otherwise. The probability of a detected hit at position x is thus described by a uniform probability function $f(x)$ on the form

$$f(x) = \begin{cases} \dfrac{1}{b-a} & \text{for } a \le x \le b \\ 0 & \text{otherwise.} \end{cases} \tag{A.7}$$

The standard deviation of this will be equal to the error in position of a particle hit in the detector segment. The standard deviation is given by

$$\sigma = \sqrt{E(X^2) - \mu^2}, \tag{A.8}$$

where $E(X)$ is the expectation value of the stochastic variable X for the probability function, and μ the mean value of the distribution. $E(X)$ is given by

$$E(X) = \int x f(x) dx = \int_a^b \frac{x}{b-a} dx = \frac{a+b}{2}. \tag{A.9}$$

This is also equal to the mean value μ. For $E(X^2)$ this becomes

$$E(X^2) = \int_a^b \frac{x^2}{b-a} dx = \frac{a^2 + ab + b^2}{3}. \tag{A.10}$$

The standard deviation is thus in total

$$\sigma = \sqrt{\frac{a^2 + ab + b^2}{3} - \left(\frac{a+b}{2}\right)^2} = \sqrt{\frac{(b-a)^2}{12}}. \tag{A.11}$$

The distance between a and b is the segment length. Calling the segment length d, the segment spatial resolution thus becomes

$$\sigma_{\text{seg}} = \frac{d}{\sqrt{12}}. \tag{A.12}$$

Thus, as an estimation, a detector with a segmentation length d will have a spatial resolution of $d/\sqrt{12}$ in that direction.

A.2.2   Pointing resolution

The pointing resolution is the accuracy with which the origin vertex position of a particle can be determined by the registered hits in the detector.

To study the pointing resolution, a good approximation of how different parameters affect it can be gathered from studying a two-layer detector. The layers are finely segmented, with errors in spatial measurements of σ_1 and σ_2. The two layers are located at radii r_1 and r_2 from the point of origin of the particle, where $r_2 > r_1$. A beampipe is considered to be located at a radius r_0.

Assuming first that the position of the track on the second layer is fixed (so that $\sigma_2 = 0$ and $\sigma_1 \neq 0$), the position resolution of the reconstructed vertex is given by [17]

$$\frac{\sigma_{\text{vtx},1}}{\sigma_1} = \frac{r_2}{r_2 - r_1} \quad \Longrightarrow \quad \sigma_{\text{vtx},1} = \frac{r_2}{r_2 - r_1}\sigma_1$$

by the law of similar triangles. In the same way, assuming the position on the first layer is fixed, the position resolution of the reconstructed vertex is

$$\sigma_{\text{vtx},2} = \frac{r_1}{r_2 - r_1}\sigma_2.$$

The resolutions of the first two layers are a combination of the segmented detector spatial resolution defined in Section A.2.1, and the uncertainty introduced by multiple scattering, defined in Section A.1.2. For the first layer, the only multiple scattering term comes from the multiple scattering in the beampipe, at radius r_0. Assuming both layers have the same segmentation, giving rise to an error of σ, and adding the errors in quadrature, the first layer resolution thus becomes

$$\sigma_1 = \sqrt{\sigma^2 + (r_1 - r_0)^2 \cdot \sigma_{\theta,0}^2}. \tag{A.13}$$

The 0 in $\sigma_{\theta,0}$ here indicates that the multiple scattering comes from the beampipe. For the second layer, two multiple scattering terms are present; one from the beampipe, and one from the first layer. The resolution thus becomes

$$\sigma_2 = \sqrt{\sigma^2 + (r_2 - r_1)^2 \cdot \sigma_{\theta,1}^2 + (r_2 - r_0)^2 \cdot \sigma_{\theta,0}^2}. \tag{A.14}$$

The multiple scattering from the first layer can be assumed to be small compared to the multiple scattering from the beampipe however, leading to the approximation

$$\sigma_2 \simeq \sqrt{\sigma^2 + (r_2 - r_0)^2 \cdot \sigma_{\theta,0}^2}. \tag{A.15}$$

The total pointing resolution for the vertex position, σ_{vtx}, is given by the combination of $\sigma_{\text{vtx},1}$ and $\sigma_{\text{vtx},2}$. The multiple scattering terms are correlated however, giving rise to a third term in the expression. With the sum in quadrature, including the correlation term, the pointing resolution is given by

$$\begin{aligned}
\sigma_{\text{vtx}} &= \sqrt{\sigma_{\text{vtx},1}^2 + \sigma_{\text{vtx},2}^2 + \sigma_{\text{correlation}}} \\
&= \sqrt{\left(\frac{r_2}{r_2 - r_1}\sigma_1\right)^2 + \left(\frac{r_1}{r_2 - r_1}\sigma_2\right)^2 + \frac{2r_1 r_2}{(r_2 - r_1)^2}(r_2 - r_0)\sigma_\theta(r_1 - r_0)\sigma_\theta} \\
&= \sqrt{\frac{r_2^2 + r_1^2}{(r_2 - r_1)^2}\sigma^2 + \frac{r_2^2(r_1 - r_0)^2 + r_1^2(r_2 - r_0)^2 + 2r_1 r_2(r_2 - r_0)(r_1 - r_0)}{(r_2 - r_1)^2}\sigma_\theta^2} \\
&= \sqrt{\frac{r_2^2 + r_1^2}{(r_2 - r_1)^2}\sigma^2 + \frac{(2r_1 r_2 - (r_1 + r_2)r_0)^2}{(r_2 - r_1)^2}\sigma_\theta^2}.
\end{aligned} \tag{A.16}$$

With the assumption $r_2 \gg r_1$, this can be written

$$\sigma_{\text{vtx}} \simeq \sqrt{\left(\frac{r_1^2}{(r_2 - r_1)^2} + 1\right)\sigma^2 + (2r_1 - r_0)^2 \cdot \sigma_\theta^2}. \tag{A.17}$$

With $\sigma = d/\sqrt{12}$ where d is the segmentation size of the detector, and the multiple scattering term as $\sigma_\theta \simeq (13.6 \text{ MeV/c} \cdot \sqrt{x/X_0})/(p \cdot \beta)$ from Section A.1.2, the pointing resolution can be written

$$\sigma_{\text{vtx}} \simeq \sqrt{\left(\frac{r_1^2}{(r_2 - r_1)^2} + 1\right) \cdot \frac{d^2}{12} + (2r_1 - r_0)^2 \cdot \frac{(13.6 \text{ MeV/c})^2}{p^2 \cdot \beta^2}\frac{x}{X_0}}. \tag{A.18}$$

The last term describes the contribution from multiple scattering, and at low momenta and velocities (small p and β), this is dominant. This term also dominates at high detector thickness, as can be seen by the proportionality to x/X_0. The term also includes a part relating to the tracker barrel layout; to minimise the pointing resolution, the innermost layer should be kept as close as possible to the beampipe, to minimise $(2r_1 - r_0)^2$.

The first term dominates at higher momenta, and shows the dependence on the segmentation size d. A smaller segmentation size thus improves pointing resolution, as it reduces σ_{vtx}. The term also shows the importance of keeping r_1 small, i.e. having the innermost layer close to the vertex. There is also an inverse proportionality to the difference between r_2 and r_1, indicating that a long lever arm is desired, with the outermost layer far away from the innermost one.

This derivation is made for a two-layer detector, but the principles hold true for more layers as well. Thin detector layers with small segmentation are desired, and an innermost layer close to the beampipe with an outermost layer far away to give a long lever arm.

A.2.3   Relative momentum resolution

In order to study the relative momentum resolution of a detector, a study of $N + 1$ equally spaced detector layers gives a good indication of the behaviour [18]. The layers are placed at radii $r_0, r_1, \ldots, r_N$ from the interaction point, and will correspond to $N+1$ equally spaced measurement points of the track. The length (lever arm) of the detector is thus given by $L = r_N - r_0$, and the resolution of a detector layer is σ (given by Section A.2.1 for a segmented detector). The detector is assumed to be in a magnetic field B, directed along the beam direction of the accelerator.

The total relative momentum resolution consists of two parts, summed in quadrature; one stemming from the detector layout, and one from multiple scattering within the detector. In this study, the transverse momentum p_{T} is considered, which is also the interesting momentum in the work carried out here, as it is orthogonal to the magnetic field. Calling the parts "geom" and "MS" respectively, the relative momentum resolution can be written

$$\frac{\sigma_{p_{\text{T}}}}{p_{\text{T}}} = \sqrt{\left(\frac{\sigma_{p_{\text{T}}}}{p_{\text{T}}}\right)_{\text{geom}}^2 + \left(\frac{\sigma_{p_{\text{T}}}}{p_{\text{T}}}\right)_{\text{MS}}^2}. \tag{A.19}$$

The multiple scattering part dominates at low momenta, while the first part dominates at higher momenta.

The first part, coming from the detector geometry, is given by [19]

$$\left(\frac{\sigma_{p_{\text{T}}}}{p_{\text{T}}}\right)_{\text{geom}} = p_{\text{T}} \cdot \frac{\sigma}{|q| \cdot B \cdot L^2} \cdot \sqrt{\frac{720 N^3}{(N-1)(N+1)(N+2)(N+3)}}. \tag{A.20}$$

The charge of the tracked particle is denoted q, and no assumption is made concerning the units of the different parameters.

The second part gives a contribution from multiple scattering as [19]

$$\left(\frac{\sigma_{p_{\text{T}}}}{p_{\text{T}}}\right)_{\text{MS}} = \frac{1}{|q|B}\frac{13.6 \text{ MeV/c}}{\beta}\sqrt{\frac{C_N}{X_0 L}}, \tag{A.21}$$

where $\beta = v/c$ is the velocity of the tracked particle, q its charge, and C_N a dimensionless coefficient dependent on the number of layers in the detector. The coefficient C_N is equal to 1.3 within 10 % accuracy. This part of the relative momentum resolution dominates at low momenta.

From the part stemming from the detector layout, Equation A.20, it is clear that a large lever arm L is very important for achieving good resolution. A high magnetic field also improves the resolution, as does a fine segmentation (decreasing σ). This part is also directly proportional to p_{T}, indicating that the resolution deteriorates at higher momenta. There is also a weak dependence on the number of detector layers ($\propto 1/\sqrt{N}$). More registered hits are important for the pattern recognition used in track reconstruction, however, so more layers are useful despite the weak dependence.

For the multiple scattering part presented in Equation A.21, there is no momentum dependence. This part dominates at low momenta. Again, stronger magnetic field gives a better resolution. There is also a weak dependence on the detector size, with the inverse proportionality to $\sqrt{L}$.
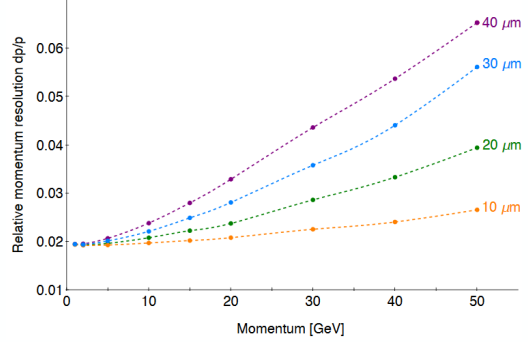
In total, relative momentum resolution improves with stronger magnetic fields and larger detectors. The formulae presented here are valid for equal spacing between detector planes, but they give a clear indication for the behaviour of a layered detector in the general case.

B   Fit interval trimming and comparison with eRD16

Comparing results of relative momentum resolution results for different pixel sizes with results of the same from eRD16, some discrepancies are found. Those are illustrated in Figure 29.
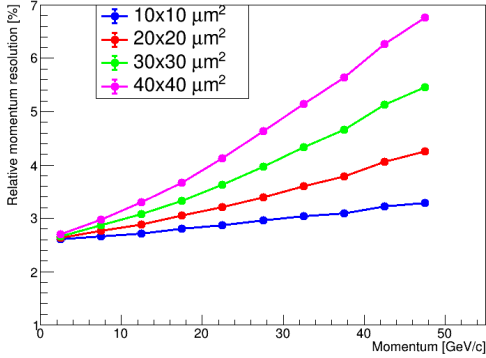
(a) University of Birmingham result.   **(b)** eRD16 result.

Figure 29: What at the time was thought to be the same simulation, carried out at different institutes with different analysis methods.

It can be seen that the eRD16 results show a better resolution at lower momenta. The trends are however the same.

The discrepancies were first thought to come from the difference in fit interval used. In eRD16, an interval of 1-3 standard deviations around the centre of the Gaussian fit is used. In the simulations done at he University of Birmingham at this time, an interval defined by a minimum value was used, resulting in a much larger fit range. Figure 30 shows a comparison to using a narrower fit interval (of 1.5 standard deviations) and the one used before.
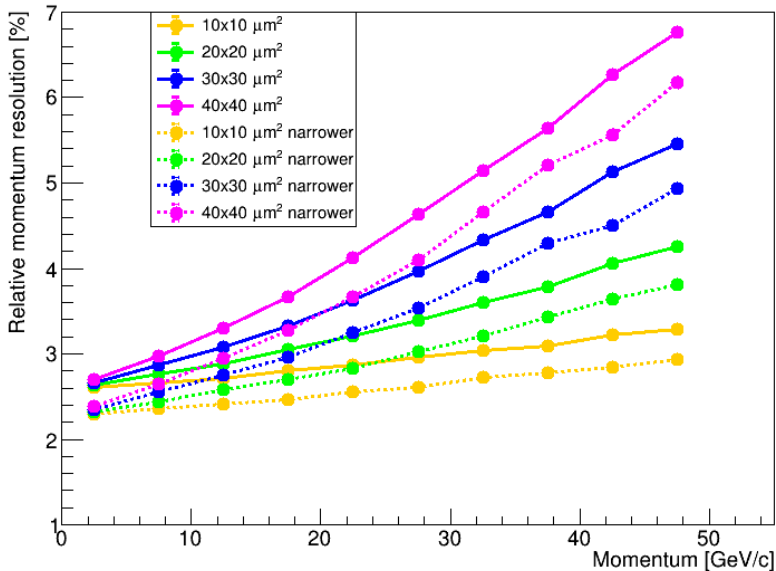

Figure 30: Comparison of fit intervals used in the data analysis. "Narrower" indicates a fit interval of 1.5 standard deviations around the peak is used.

It is quite clear that the narrower fit interval lowers the resolution. The narrower interval also

provides a more accurate fit in many cases, so it is used throughout this report.

Since this study, it has also come to light that eRD16 used a different magnetic field map in the simulations carried out. This field map was not uniform, which again introduces discrepancies compared to the simulations in uniform magnetic field maps done at the University of Birmingham.

C   Further gas TPC replacement studies

C.1   Different silicon layouts

In addition to the studies presented in Section 3.9, a few further layouts are investigated. The simulation parameters used are shown below.

- Particle: e^-

- Momentum range: 0 to 50 GeV/c (uniform in p)

- $0 \leq \eta \leq 2.5$

- Number of events: 100 000

- Pixel size: 20×20 μm^2

- Magnetic field: 1.5 T

First of all reference runs are shown, using no TPC (*No TPC; standard disks*), and the standard TPC (*With gas TPC*) with the regular basic disks. The first gas TPC replacement layout tested here is having two silicon layers (*2 layers, long*) with a thickness of 0.8 % X_0 and a length of 1960 mm, the first one at the innermost TPC radius (225.0 mm) and the second at the outermost TPC radius (775.0 mm). This layout is not part of the main results, as having only two layers will make associating hits to tracks difficult due to the large empty volume between them. A simulation is also done for a 12 layer layout, filling the space the gas TPC occupies with 12 silicon layers, placed 46.2 mm apart (*12 layers, long*). This layout is not part of the main results due to the large material thickness 12 layers give.

Layouts with shorter (840 mm) layer length and enlarged disk radii are also tested. A result is shown for no TPC with disks of radius 420.0 mm (*No TPC; large disks*), for a two-layer layout with the same disks (*2 layers, short; large disks*), and also for a two-layer layout with disks extending all the way out to a radius of 775.0 mm (*2 layers, short; very large disks*). Disks this big are likely not physically viable, which is why this is not part of the main results.

Resolutions from the simulations are shown in Figure 31 versus momentum, and in Figure 32 versus pseudorapidity. The longitudinal pointing resolutions do not change significantly between the layouts, and are thus not shown.
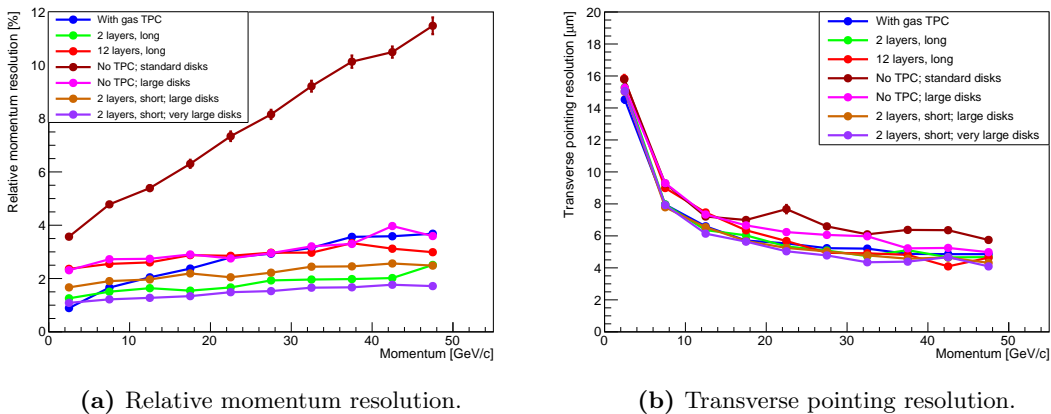
(a) Relative momentum resolution.

(b) Transverse pointing resolution.

Figure 31: Relative momentum resolution and transverse pointing resolution versus momentum for different gas TPC replacement configurations.

Looking at the relative momentum resolution versus momentum, it can first of all be seen that the disk size has a large effect. Comparing the no TPC runs, having 420.0 mm large disks radically improves the resolution. It can also be seen that the 12 layer layout does not have better momentum resolution than the gas TPC at momenta below 38 GeV/c, due to the large
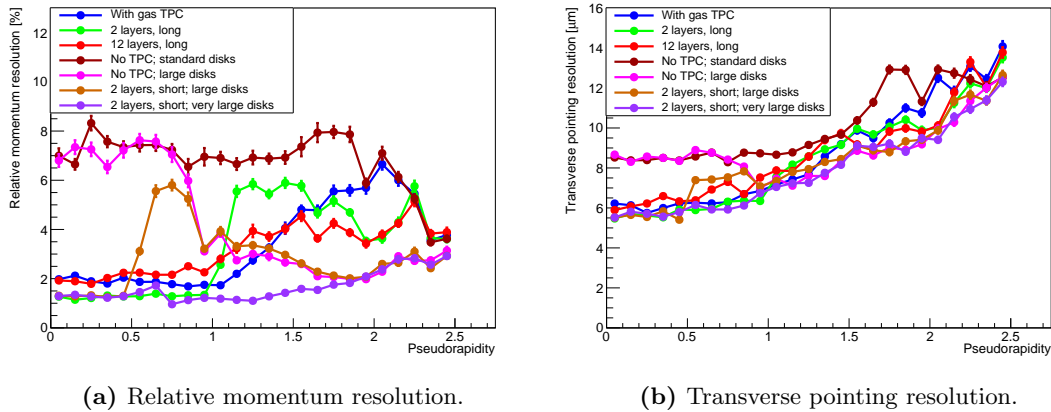
(a) Relative momentum resolution.   (b) Transverse pointing resolution.

Figure 32: Relative momentum resolution and transverse pointing resolution versus pseudorapidity for different gas TPC replacement configurations.

amount of material. The layout with two layers and disks of radius 775.0 mm has the best momentum resolution everywhere. This is due to the full coverage in all of the investigated pseudorapidity range. The optimised disk layout described in Section 3.9 attempts to recreate this in a feasible way.

The transverse pointing resolution is not significantly different for the layouts where there is silicon replacing the gas TPC, apart from for the 12 layer layout, which is worse than the others up to momenta of 28 GeV/c. This is again due to the large amount of material giving rise to multiple scattering. The runs without gas TPC or silicon replacement have slightly worse pointing resolution than the others, likely due to the significant decrease in lever arm length at central pseudorapidities.

Looking at the plots versus pseudorapidity, there are clear ridges where the disks come into play. In the relative momentum resolution plot, comparing the no TPC runs, it can be seen that the standard disks do not improve the resolution until $\eta \geq 1.7$. For the 420.0 mm radius disks, this happens already at $\eta \geq 0.9$. It can again be seen that the disk size has a large effect. The layout with no TPC and 420.0 mm disks outperform the gas TPC layout (with standard disks) at $\eta \geq 1.3$. The disks with a radius of 775.0 mm keep the momentum resolution low throughout the investigated pseudorapidity range.

The effect of the disk radius can also be seen in the same way in the plot of transverse pointing resolution versus pseudorapidity. It can also be seen that having full detector coverage (as is the case with the 775.0 mm disks) is beneficial. This is the conclusion leading to the optimised disk layout.

C.1.1   Comparison of two silicon layers and five silicon layers

A study is also made comparing two-layer layouts with five-layer layouts, to see whether five layers deteriorates the resolutions. Both 420 mm disks and the optimised disk layout are tested. Results of this study are shown in Figure 33 versus momentum, and in Figure 34 versus pseudorapidity. There is no significant difference in the longitudinal pointing resolution, and those plots are thus not shown.

From this, it can be seen that having five silicon layers instead of two is not severely detrimental to any of the resolutions in this parameter space. Five layers will however help with track reconstruction, and this layout is thus more beneficial than the two layer layout. This is therefore the layout presented as part of the main results in Section 3.9.
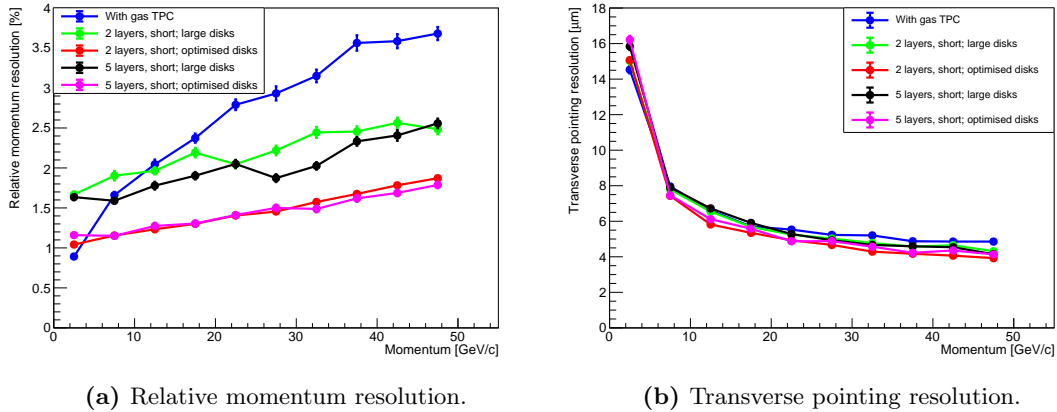
(a) Relative momentum resolution.

(b) Transverse pointing resolution.

Figure 33: Relative momentum resolution and transverse pointing resolution versus momentum for 2 and 5 layers in the TPC replacement silicon barrel.

(a) Relative momentum resolution.
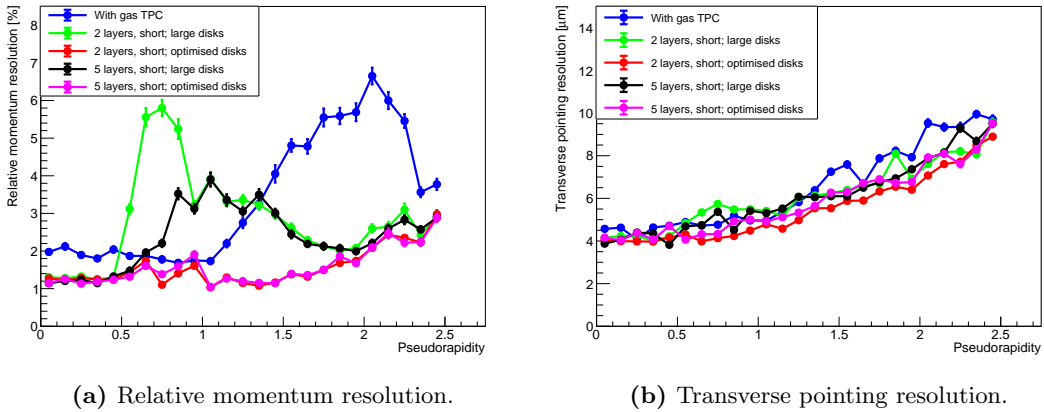
(b) Transverse pointing resolution.

Figure 34: Relative momentum resolution and transverse pointing resolution versus pseudorapidity for 2 and 5 layers in the TPC replacement silicon barrel.

C.2   Different silicon replacement outer radius

For the study of different silicon layout radii, the results from using disks with a radius of 420.0 mm (instead of the optimised disk layout) are presented here. The sudy is made in a pseudorapidity interval of $1 \leq \eta \leq 2.5$. Figures 35 and 36 show the resolutions versus momentum and pseudorapidity respectively.

From Figure 35, it can be seen that in this forward region, the five layer layout with 420 mm radius disks outperforms the gas TPC at momenta above approximately 5 GeV/c, for all the tested radii. The pointing resolutions show no significant difference at any momentum.

In Figure 36, it can be seen that the silicon layouts all are very similar (since the disks dominate in the largest part of this region), and have better relative momentum resolution than the gas TPC at pseudorapidities exceeding 1.35, regardless of the outer radius. The transverse pointing resolution for the gas TPC is worse than the silicon layouts at pseudorapidities between 1.5 and 2.3.
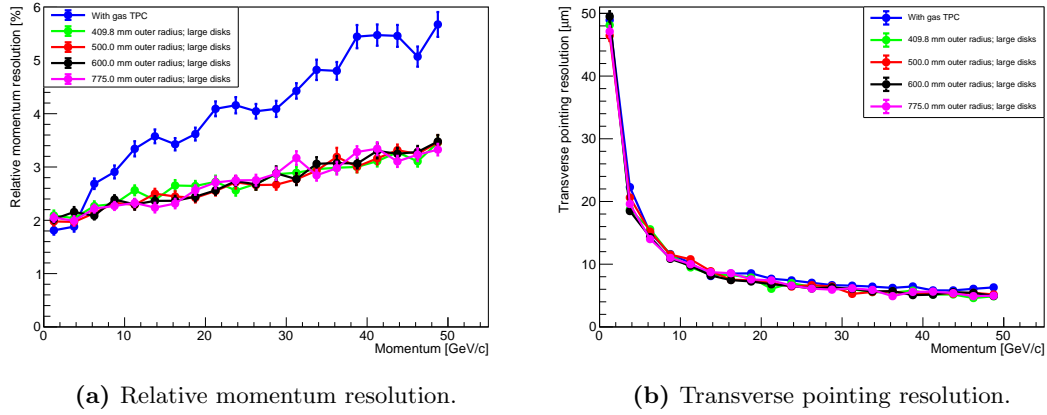
(a) Relative momentum resolution.

(b) Transverse pointing resolution.

Figure 35: Relative momentum resolution and transverse pointing resolution versus momentum for different silicon TPC replacement outer radii, with 420 mm radius disks. Forward regions ($1 \leq \eta \leq 2.5$).
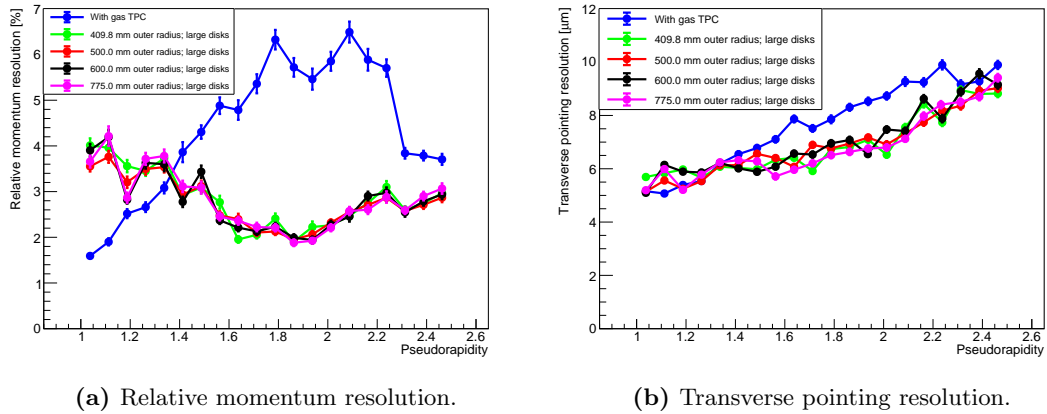

(a) Relative momentum resolution.

(b) Transverse pointing resolution.

Figure 36: Relative momentum resolution and transverse pointing resolution versus pseudorapidity for different silicon TPC replacement outer radii, with 420 mm radius disks. Forward regions ($1 \leq \eta \leq 2.5$).

D   Area comparison to the ALICE ITS Upgrade

In order to get an approximation of the cost of the silicon vertex tracker, a silicon area comparison is made with the ALICE ITS Upgrade [5]. The area of the seven silicon barrel layers in the ALICE ITS Upgrade is approximately 9.3 m^2 [5]. The five barrel layers in the design presented in this report (two inner layers, two outer layers, one time-stamping layer) have a total area of approximately 2.5 m^2. Hence, the silicon barrel presented here has an area 27 % that of the ALICE ITS Upgrade barrel.

If the gas TPC is replaced with 5 silicon layers, the total silicon area will depend on the radii the layers are located at. Table 2 gives a summary for the radii discussed in Section 3.9, with layers being 840 mm long. If they are instead 1960 mm long, the areas will increase by a factor of $1960/840 \approx 2.33$.

Outer radius	Area of Si TPC repl. + barrel	% of ALICE ITS
Barrel only	2.51 m^2	26.7 %
409.8 mm	10.9 m^2	117 %
500.0 mm	12.1 m^2	130 %
600.0 mm	13.4 m^2	144 %
775.0 mm	15.7 m^2	169 %

Table 2: Five layer silicon TPC replacement areas, compared to the ALICE ITS Upgrade. Disks are not included.

The standard disks used (7 forward, 7 backward) have a total area of approximately 1.4 m^2. The baseline layout, as shown in Figure 2, thus has an area approximately 42 % that of the ITS Upgrade barrel.

If the disks have a radius of 420 mm, the total silicon area from the disks becomes approximately 6.7 m^2, which is approximately 72 % of the area of the ALICE ITS Upgrade barrel.

In the optimised disk layout, the total disk area will again depend on the outer radius of the tracker. Table 3 summarises the disk area for different outer radii, and its comparison with the ALICE ITS Upgrade barrel.

Outer radius	Area of silicon disks	% of ALICE ITS
409.8 mm	3.71 m^2	39.9 %
500.0 mm	5.77 m^2	62.0 %
600.0 mm	8.53 m^2	91.8 %
775.0 mm	14.6 m^2	157 %

Table 3: Optimised disk area for different outer radii, compared to the ALICE ITS Upgrade barrel.

References

[1] A. Kiselev. EIC Generic Detector R&D: tracking applications, July 2018. EIC Tracking Workshop. (Cited on p. 3.)

[2] G. Wei, F. Lin, V. Morozov, et al. Integration of the full-acceptance detector into the JLEIC. In *8th Int. Particle Accelerator Conf.(IPAC'17), Copenhagen, Denmark, 14-19 May, 2017*, pages 3912–3914. JACOW, Geneva, Switzerland, 2017. (Cited on p. 3.)

[3] PHENIX Collaboration, A. Adare, C. Aidala, et al. Concept for an Electron Ion Collider (EIC) detector built around the BaBar solenoid. *ArXiv e-prints*, February 2014. (Cited on p. 3 and 5.)

[4] J. Repond. PID with fast silicon, July 2018. EIC User Group Meeting. (Cited on p. 3.)

[5] B. Abelev, J. Adam, D. Adamová, et al. Technical Design Report for the Upgrade of the ALICE Inner Tracking System. Technical Report CERN-LHCC-2013-024. ALICE-TDR-017, Nov 2013. (Cited on p. 3, 6, and 42.)

[6] A. Kiselev and eRHIC task force team. EIC detector simulations in FairRoot framework. In *APS Division of Nuclear Physics Meeting Abstracts*, page DG.004. October 2013. (Cited on p. 5.)

[7] M. Al-Turany, D. Bertini, R. Karabowicz, et al. The FairRoot framework. *Journal of Physics: Conference Series*, 396(2):022001, 2012. (Cited on p. 5.)

[8] A. Accardi, J. Albacete, M. Anselmino, et al. Electron Ion Collider: The Next QCD Frontier-Understanding the glue that binds us all. *arXiv preprint arXiv:1212.1701*, 2012. (Cited on p. 5 and 25.)

[9] JLEIC Design Study Collaboration, T. Satogata, and Y. Zhang. JLEIC - A Polarized Electron-Ion Collider at Jefferson Lab. *ICFA Beam Dyn. Newslett.*, 74:92–182, 2018. (Cited on p. 5.)

[10] R. Frühwirth. Application of Kalman filtering to track and vertex fitting. *Nuclear Instruments and Methods in Physics Research Section A: Accelerators, Spectrometers, Detectors and Associated Equipment*, 262(2):444 – 450, 1987. ISSN 0168-9002. doi:https://doi.org/10.1016/0168-9002(87)90887-4. (Cited on p. 5.)

[11] eRD16 collaboration presentation. Forward/Backward Tracking at EIC using MAPS Detectors, July 2018. EIC Detector R&D Advisory Committee meeting. (Cited on p. 14.)

[12] B. R. Martin. *Nuclear and Particle Physics*. John Wiley & Sons Ltd, 2nd edition, 2012. ISBN 978-0-470-74275-4. (Cited on p. 31.)

[13] W. R. Leo. *Techniques for Nuclear and Particle Physics Experiments*. Springer-Verlag, 2nd edition, 1994. ISBN 0-387-17386-2. (Cited on p. 31.)

[14] H. A. Bethe. Molière's Theory of Multiple Scattering. *Phys. Rev.*, 89:1256–1266, Mar 1953. doi:10.1103/PhysRev.89.1256. (Cited on p. 31.)

[15] V. L. Highland. Some practical remarks on multiple scattering. *Nuclear Instruments and Methods*, 129(2):497 – 499, 1975. ISSN 0029-554X. doi:https://doi.org/10.1016/0029-554X(75)90743-0. (Cited on p. 31.)

[16] G. R. Lynch and O. I. Dahl. Approximations to multiple Coulomb scattering. *Nuclear Instruments and Methods in Physics Research Section B: Beam Interactions with Materials and Atoms*, 58(1):6 – 10, 1991. ISSN 0168-583X. doi:https://doi.org/10.1016/0168-583X(91)95671-Y. (Cited on p. 31.)

[17] N. Wermes. Pixel vertex detectors. In *Proceedings, 34th SLAC Summer Institute on Particle Physics: The Next Frontier: Exploring with the LHC (SSI 2006): Menlo Park, California*. July 2006. (Cited on p. 33.)

[18] R. Gluckstern. Uncertainties in track momentum and direction, due to multiple scattering and measurement errors. *Nuclear Instruments and Methods*, 24:381 – 389, 1963. ISSN 0029-554X. doi:https://doi.org/10.1016/0029-554X(63)90347-1. (Cited on p. 34.)

[19] F. Ragusa and L. Rolandi. Tracking at LHC. *New Journal of Physics*, 9(9):336, 2007. (Cited on p. 34.)